

# BlackMax: A black-hole event generator with rotation, recoil, split branes and brane tension.

De-Chang Dai<sup>1</sup>, Glenn Starkman<sup>1</sup>, Dejan Stojkovic<sup>2</sup>, Cigdem Issever<sup>3</sup>, Eram Rizvi<sup>4</sup>, Jeff Tseng<sup>3</sup>

<sup>1</sup>Case Western Reserve University, Cleveland OH 44106-7079, USA

<sup>2</sup>Department of Physics, SUNY at Buffalo, Buffalo NY 14260-1500, USA

<sup>3</sup>University of Oxford, Oxford, UK and

<sup>4</sup>Queen Mary, University of London, London, UK

---

We present a comprehensive black-hole event generator, BlackMax, which simulates the experimental signatures of microscopic and Planckian black-hole production and evolution at the LHC in the context of brane world models with low-scale quantum gravity. The generator is based on phenomenologically realistic models free of serious problems that plague low-scale gravity, thus offering more realistic predictions for hadron-hadron colliders. The generator includes all of the black-hole gray-body factors known to date and incorporates the effects of black-hole rotation, splitting between the fermions, non-zero brane tension and black-hole recoil due to Hawking radiation (although not all simultaneously).

The generator can be interfaced with Herwig and Pythia.

The main code can be downloaded from [1].

PACS numbers: 04.50.Gh, 04.70.Dy

## I. INTRODUCTION

Models with TeV-scale quantum gravity [2, 3, 4, 5] offer very rich collider phenomenology. Most of them assume the existence of a three-plus-one-dimensional hypersurface, which is referred as “the brane,” where Standard-Model particles are confined, while only gravity and possibly other particles that carry no gauge quantum numbers, such as right handed neutrinos can propagate in the full space, the so called “bulk”. Under certain assumptions, this setup allows the fundamental quantum-gravity energy scale,  $M_*$ , to be close to the electroweak scale. The observed weakness of gravity compared to other forces on the brane (*i.e.* in the laboratory) is a consequence of the large volume of the bulk which dilutes the strength of gravity.

In the context of these models of TeV-scale quantum gravity, probably the most exciting new physics is the production of micro-black-holes in near-future accelerators like the Large Hadron Collider (LHC) [6]. According to the “hoop conjecture” [7], if the impact parameter of two colliding particles is less than two times the gravitational radius,  $r_h$ , corresponding to their center-of-mass energy ( $E_{CM}$ ), a black-hole with a mass of the order of  $E_{CM}$  and horizon radius,  $r_h$ , will form. Typically, this gravitational radius is approximately  $E_{CM}/M_*^2$ . Thus, when particles collide at center-of-mass energies above  $M_*$ , the probability of black-hole formation is high.

Strictly speaking, there exist no complete calculation (including radiation during the process of formation and back-reaction) which proves that a black-hole really forms. It may happen that a true event horizon

and singularity never forms, and that Hawking (or rather Hawking-like) radiation is never quite thermal. In [8] this question was analyzed in detail from a point of view of an asymptotic observer, who is in the context of the LHC the most relevant observer. It was shown that though such observers never observe the formation of an event horizon even in the full quantum treatment, they do register pre-Hawking quantum radiation that takes away energy from a collapsing system. Pre-Hawking radiation is non-thermal and becomes thermal only in the limit when the horizon is formed. Since a collapsing system has only a finite amount of energy, it disappears before the horizon is seen to be formed. While these results have important implications for theoretical issues like the information loss paradox, in a practical sense very little will change. The characteristic time for gravitational collapse in the context of collisions of particles at the LHC is very short. This implies that pre-Hawking radiation will be quickly experimentally indistinguishable from Hawking radiation calculated for a real black hole. Also, calculations in [8] indicate that the characteristic time in which a collapsing system losses all of its energy is very similar to a life time of a real black-hole. Thus, one may proceed with a standard theory of black-holes.

Once a black-hole is formed, it is believed to decay via Hawking radiation. This Hawking radiation will consist of two parts: radiation of Standard-Model particles into the brane and radiation of gravitons and any other bulk modes into the bulk. The relative probability for the emission of each particle type is given by the gray-body factor for that mode. This gray-body factor depends on the properties of the particle (charge, spin, mass, momen-

tum), of the black-hole (mass, spin, charge) and, in the context of TeV-scale quantum gravity, on environmental properties – the number of extra dimensions, the location of the black-hole relative to the brane (or branes), *etc.*. In order to properly describe the experimental signatures of black-hole production and decay one must therefore calculate the gray-body factors for all of the relevant degrees of freedom.

There are several black-hole event generators available in the literature [9] based on particular, simplified models of low-scale quantum gravity and incorporating limited aspects of micro-black-hole physics. Unfortunately, low-scale gravity is plagued with many phenomenological challenges like fast proton decay, large  $n\bar{n}$  oscillations, flavor-changing neutral currents and large mixing between leptons [10, 11]. For a realistic understanding of the experimental signature of black hole production and decay, one needs calculations based on phenomenologically viable gravity models, and incorporating all necessary aspects of the production and evolution of the black-holes.

One low-scale gravity model in which the above mentioned phenomenological challenges can be addressed is the split-fermion model [12]. In this model, the Standard Model fields are confined to a “thick brane”, much thicker than  $M_*^{-1}$ . Within this thick brane, quarks and leptons are stuck on different three-dimensional slices (or on different branes), which are separated by much more than  $M_*^{-1}$ . This separation causes an exponential suppression of all direct couplings between quarks and leptons, because of exponentially small overlaps between their wave-functions. The proton decay rate will be safely suppressed if the spatial separation between quarks and leptons is greater by a factor of at least 10 than the widths of their wave functions. Since  $\Delta B = 2$  processes, like  $n\bar{n}$  oscillations, are mediated by operators of the type  $uddd$ , suppressing them requires a further splitting between up-type and down-type quarks. Since the experimental limits on  $\Delta B = 2$  operators are much less stringent than those on  $\Delta B = 1$  operators, the u and d-type quarks need only be separated by a few times the width of their wave functions [12].

Current black-hole generators assume that the black-holes that are formed are Schwarzschild-like. However, most of the black-holes that would be formed at the LHC would be highly rotating, due to the non-zero impact parameter of the colliding partons. Due to the existence of an ergosphere (a region between the infinite redshift surface and the event horizon), a rotating black-hole exhibits super-radiance: some modes of radiation get amplified compared to others. The effect of super-radiance [13] is strongly spin-dependent, with emission of higher-spin particles strongly favored. In particular the emission of gravitons is enhanced over lower-spin Standard-Model particles. Since graviton emission appears in detectors as missing energy, the effects of black-hole rotation cannot

be ignored. Similarly, black-holes may be formed with non-zero gauge charge, or acquire charge during their decay. This again may alter the decay properties of the black-hole and should be included.

Another effect neglected in other generators is the recoil of the black-hole. A small black-hole attached to a brane in a higher-dimensional space emitting quanta into the bulk could leave the brane as a result of a recoil<sup>1</sup>. In this case, visible black-hole radiation would cease. Alternatively, in a split-brane model, as a black-hole traverses the thick brane the Standard-Model particles that it is able to emit will change depending on which fermionic branes are nearby.

It is also the case that virtually all the work in this field has been done for the idealized case where the brane tension is negligible. However, one generically expects the brane tension to be of the order of the fundamental energy scale, being determined by the vacuum energy contributions of brane-localized matter fields[14]. As shown in [15], finite brane tension modifies the standard gray-body factors.

Finally, it has been suggested [16] that more common than the formation and evaporation of black-holes will be gravitational scattering of parton pairs into a two-body final state. We include this possibility.

Here we present a comprehensive black-hole event generator, BlackMax, that takes into account practically all of the above mentioned issues<sup>2</sup>, and includes almost all the necessary gray-body factors<sup>3</sup>. Preliminary studies show how the signatures of black-hole production and decay change when one includes splitting between the fermions, black-hole rotation, positive brane tension and black-hole recoil. Future papers will explore the implications of these changes in greater detail.

In section II and III we discuss the production of black-holes and the gray-body factors respectively. The evaporation process and final burst of the black-holes is discussed in section IV and V. Sections VI and describe the input and output of the generator. Section VII shows some characteristic distributions of black-holes for different extra dimension scenarios. The reference list is extensive, reflecting the great interest in the topic [6, 7, 9, 10, 11, 14, 15, 16, 17, 18, 19, 20, 21, 22, 23, 24, 25, 27, 28, 29, 30, 31, 33, 34, 35, 36, 37, 38, 39, 40, 41, 42, 43, 44, 45, 46, 47, 48, 49, 50, 51, 52, 53, 54, 55, 56, 57, 58, 59, 60, 61, 62, 63, 64, 65, 66, 67, 68, 69, 70, 71, 72, 73, 74, 75, 76, 77, 78, 79, 80, 81, 82, 83, 84, 85, 86, 87, 88, 89, 90, 91, 92, 93, 94, 95, 96, 97, 98, 99, 100, 101, 102, 103, 104, 105, 106, 107], but by no means complete.

<sup>1</sup> Although if the black-hole carries gauge charge it will be prevented from leaving the brane.

<sup>2</sup> although not necessarily simultaneously

<sup>3</sup> Except in the one case of the graviton gray-body factor for a rotating black-hole, where the calculation has yet to be achieved.

## II. BLACK-HOLE PRODUCTION

We assume that the fundamental quantum-gravity energy scale  $M_*$  is not too far above the electroweak scale. Consider two particles colliding with a center-of-mass energy  $E_{CM}$ . They will also have an angular momentum  $J$  in their center-of-mass (CM) frame. By the hoop conjecture, if the impact parameter,  $b$ , between the two colliding particles is smaller than the diameter of the horizon of a  $(d+1)$ -dimensional black-hole (where  $d$  is the total number of space-like dimensions) of mass  $M = E_{CM}$  and angular momentum  $J$ ,

$$b < 2r_h(d, M, J), \quad (1)$$

then a black-hole with  $r_h$  will form. The cross section for this process is approximately equal to the interaction area  $\pi(2r_h)^2$ .

In Boyer-Lindquist coordinates, the metric for a  $(d+1)$ -dimensional rotating black-hole (with angular momentum parallel to the  $\hat{\omega}$  in the rest frame of the black-hole) is:

$$\begin{aligned} ds^2 = & \left(1 - \frac{\mu r^{4-d}}{\Sigma(r, \theta)}\right) dt^2 \\ & - \sin^2 \theta \left( r^2 + a^2 \left( + \sin^2 \theta \frac{\mu r^{4-d}}{\Sigma(r, \theta)} \right) \right) d\phi^2 \\ & + 2a \sin^2 \theta \frac{\mu r^{4-d}}{\Sigma(r, \theta)} dt d\phi - \frac{\Sigma(r, \theta)}{\Delta} dr^2 \\ & - \Sigma(r, \theta) d\theta^2 - r^2 \cos^2 \theta d^{d-3} \Omega \end{aligned} \quad (2)$$

where  $\mu$  is a parameter related to mass of the black-hole, while

$$\Sigma = r^2 + a^2 \cos^2 \theta \quad (3)$$

and

$$\Delta = r^2 + a^2 - \mu r^{4-d}. \quad (4)$$

The mass of the black-hole is

$$M = \frac{(d-1)A_{d-1}}{16\pi G_d} \mu, \quad (5)$$

and

$$J = \frac{2Ma}{d-1} \quad (6)$$

is its angular momentum. Here,

$$A_{d-1} = \frac{2\pi^{d/2}}{\Gamma(d/2)} \quad (7)$$

is the hyper-surface area of a  $(d-1)$ -dimensional unit sphere. The higher-dimensional gravitational constant  $G_d$  is defined as

$$G_d = \frac{\pi^{d-4}}{4M_*^{d-1}}. \quad (8)$$

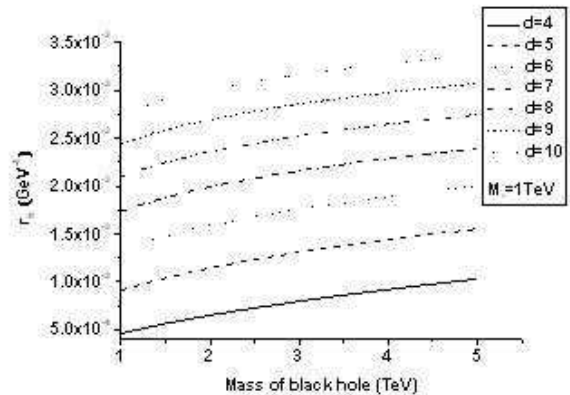


FIG. 1: Horizon radius (in  $\text{GeV}^{-1}$ ) of a non-rotating black-hole as a function of mass for 4-10 spatial dimensions.

The horizon occurs when  $\Delta = 0$ . That is at a radius given implicitly by

$$r_h^{(d)} = \left[ \frac{\mu}{1 + (a/r_h^{(d)})^2} \right]^{\frac{1}{d-2}} = \frac{r_s^{(d)}}{\left[ 1 + (a/r_h^{(d)})^2 \right]^{\frac{1}{d-2}}}. \quad (9)$$

Here

$$r_s^{(d)} \equiv \mu^{1/(d-2)} \quad (10)$$

is the Schwarzschild radius of a  $(d+1)$ -dimensional black-hole, *i.e.* the horizon radius of a non-rotating black-hole. Equation 10 can be rewritten as:

$$r_s^{(d)}(E_{CM}, d, M_*) = k(d) M_*^{-1} [E_{CM}/M_*]^{1/(d-2)}, \quad (11)$$

where

$$k(d) \equiv \left[ 2^{d-3} \pi^{(d-6)/2} \frac{\Gamma[d/2]}{d-1} \right]^{1/(d-2)}. \quad (12)$$

Figure 1 shows the horizon radius as a function of black-hole mass for  $d$  from 4 to 10. We see that the horizon radius increases with mass; it also increases with  $d$ . Figure 2 shows the Hawking temperature of a black-hole

$$T_H = \frac{d-2}{4\pi r_h} \quad (13)$$

as a function of the black-hole mass for  $d$  from 4 to 10. The Hawking temperature is a measure of the characteristic energies of the particles emitted by the black-hole.  $T_H$  decreases with increasing mass. However, the behaviour of  $T_H$  with changing  $d$  is complicated, reflecting the competing effect of an increasing horizon radius and an increasing  $d-2$  in equation 13.

For the model with non-zero tension brane, the radius of the black-hole is defined as

$$r_h^{(t)} = \frac{r_s}{B^{1/3}}, \quad (14)$$

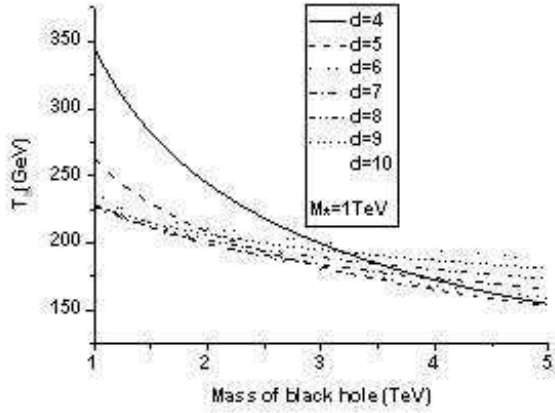


FIG. 2: Hawking temperature(in GeV) of a non-rotating black-hole as a function of mass for 4-10 spatial dimensions.

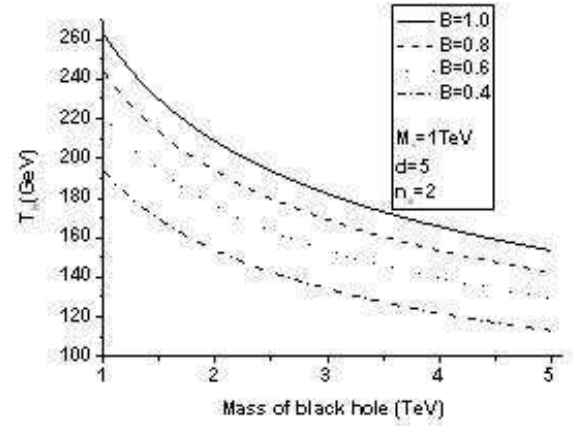


FIG. 4: Hawking temperature(in GeV) of a black-hole as a function of mass for different B in d=5 spatial dimensions.

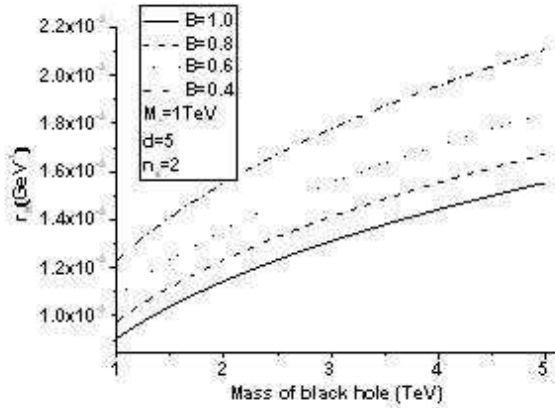


FIG. 3: Horizon radius (in  $\text{GeV}^{-1}$ ) of a black-hole as a function of mass for different B in d=5 spatial dimensions.

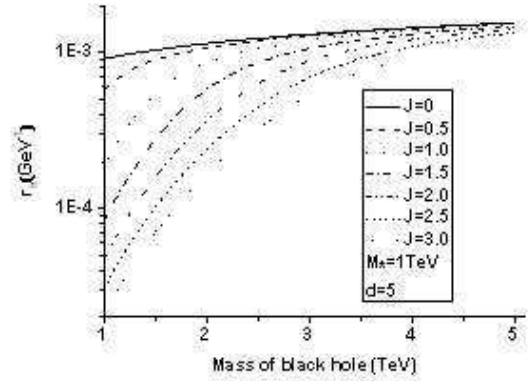


FIG. 5: Horizon radius (in  $\text{GeV}^{-1}$ ) of a rotating black-hole as a function of mass for different angular momentum in d=5 spatial dimensions. Angular momentum J is in unit of  $\hbar$ .

with  $B$  the deficit-angle parameter which is inverse proportional to the tension of the brane.

Figure 3 shows the horizon radius as a function of black-hole mass for the model with non-zero tension brane. As the deficit-angle parameter increases, the size of the black-hole increases.

Figure 4 shows the Hawking temperature of a black-hole for the model with non-zero tension brane. The Hawking temperature decreases as the deficit angle decreases.

Figure 5 shows the horizon radius as a function of black-hole mass for a rotating black-hole. The angular momentum decreases the size of the horizon and increases the Hawking temperature (see figures 5 and 6).

If two highly relativistic particles collide with center-of-mass energy  $E_{CM}$ , and impact parameter  $b$ , then their angular momentum in the center-of-mass frame before the collision is  $L_{in} = bE_{CM}/2$ . Suppose for now that

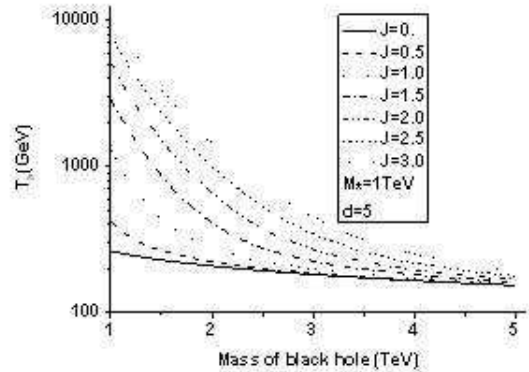


FIG. 6: Hawking temperature(in GeV) of a rotating black-hole as a function of mass for different angular momentum in d=5 spatial dimensions. Angular momentum J is in unit of  $\hbar$ .

the black-hole that is formed retains all this energy and angular momentum. Then the mass and angular momentum of the black-hole will be  $M_{in} = E_{CM}$  and  $J_{in} = L_{in}$ . A black-hole will form if:

$$b < b_{max} \equiv 2r_h^{(d)}(E_{CM}, b_{max}E_{CM}/2). \quad (15)$$

We see that  $b_{max}$  is a function of both  $E_{CM}$  and the number of extra dimensions.

We can rewrite condition (15) as

$$b_{max}(E_{CM}; d) = 2 \frac{r_s^{(d)}(E_{CM})}{\left[1 + \left(\frac{d-1}{2}\right)^2\right]^{\frac{1}{d-2}}}. \quad (16)$$

There is one exception to this condition. In the case where we are including the effects of the brane tension, the metric (and hence gray-body factors) for a rotating black-hole are not known. In this case we consider only non-rotating black-holes. Therefore, for branes with tension

$$b_{max}^{tension}(E_{CM}, d) = 2r_s^{(d)}(E_{CM}). \quad (17)$$

Also, for branes with tension only the  $d = 5$  metric is known.

At the LHC, each proton will have  $E = 7$  TeV in the CM frame. Therefore, the total proton-proton center of mass energy will be  $\sqrt{s} = 14$  TeV. However, it is not the protons that collide to make the black-holes, but the partons of which the protons are made. If two partons have energy  $vE$  and  $\frac{uE}{v}$ , much greater than their respective masses, then the parton-parton collision will have

$$s' = |p_i + p_j|^2 = |v(E, E) + \frac{u}{v}(E, -E)|^2 = 4uE^2 = us. \quad (18)$$

We define a quantity  $Q'$

$$Q' = E_{CM} = \sqrt{s'} = \sqrt{us} \quad (19)$$

The center-of-mass energy for the two colliding partons will be  $\sqrt{us}$ , as will be the 4-momentum transfer  $Q'^2$ . The largest impact parameter between the two partons that can form a black-hole with this mass will therefore be  $b_{max}(\sqrt{us}; d)$ , as given by equation 16.

The total proton-proton cross section for black-hole production is therefore

$$\begin{aligned} \sigma^{pp \rightarrow BH}(s; d, M_*) &= \int_{M_*^2/s}^1 du \int_u^1 \frac{dv}{v} \pi [b_{max}(\sqrt{us}; d)]^2 \\ &\times \sum_{ij} f_i(v, Q') f_j(u/v, Q'). \end{aligned} \quad (20)$$

Here  $f_i(v, Q')$  is the  $i$ -th parton distribution function. Loosely this is the expected number of partons of type  $i$  and momentum  $vE$  to be found in the proton in a collision at momentum transfer  $Q'$ .

In [16] it is argued that strong gravity effects at energies close to the Planck scale will lead to an increase in the  $2 \rightarrow 2$  cross section via the exchange of Planckian ‘‘black-holes’’ (by which any quantum gravity effect or resonance is meant). Final states with high multiplicities are predicted to be suppressed. Although the intermediate state is created in the strong gravity regime, it is not a conventional microscopic black hole. The state is not stable. Thermal Hawking radiation does not take place. Especially since inelastic collisions increase the energy loss, the threshold for creating stable black-holes shifts to even higher values. Thus  $2 \rightarrow 2$  scattering may be the most important signal in the LHC instead of black-holes evaporating via Hawking radiation. One should find that the cross section for two-body final states suddenly jumps to a larger value, as the energy reaches the quantum-gravity scale. We calculate the cross section of two-body final states by replacing  $\pi b_{max}^2$  in equation (20) with

$$\pi b_{max}(\sqrt{s'} > M_{min})^2 \approx \pi r_s^2 P_2 \quad (21)$$

where

$$P_2 = e^{-\langle N \rangle} \sum_{i=0}^2 \frac{\langle N \rangle^i}{i!} \quad (22)$$

$$\langle N \rangle = \rho \left( \frac{4\pi k(d) M_{BH}}{d-1 M_*} \right)^{(d-1)/(d-2)} \quad (23)$$

$$\rho = \frac{\sum c_i g_i \Gamma_i \zeta(3) \Gamma(3)}{\sum c_i f_i \Phi_i \zeta(4) \Gamma(4)} \quad (24)$$

$$\Gamma_i = \frac{1}{4\pi r^2} \int \frac{\sigma_i(\omega) \omega^2 d\omega}{e^{\omega/T} \pm 1} \left[ \int \frac{\omega^2 d\omega}{e^{\omega/T} \pm 1} \right]^{-1} \quad (25)$$

$$\Phi_i = \frac{1}{4\pi r^2} \int \frac{\sigma_i(\omega) \omega^3 d\omega}{e^{\omega/T} \pm 1} \left[ \int \frac{\omega^3 d\omega}{e^{\omega/T} \pm 1} \right]^{-1} \quad (26)$$

Here  $c_i$  is the number of internal degrees of freedom of particle species  $i$ ,  $g_i = 1$  and  $f_i = 1$  for bosons, and  $g_i = 3/4$  and  $f_i = 7/8$  for fermions [28].

Figure 7 shows the cross section for non-rotating black-holes on a tensionless brane as a function of mass for different numbers of spatial dimensions. The cross section increases with the number of spatial dimensions.

Figure 8 shows the cross section for non-rotating black holes on a brane with positive tension as a function of mass for various deficit angle parameter,  $B$ . The cross section increases as the tension increases (as  $B$  decreases).

Figure 9 shows the cross section for non-rotating black holes as function of the number of split-fermion space dimensions,  $n_s$ . When a pair of partons are separated in the extra-dimensions they must approach more closely in the ordinary dimensions in order to form a black-hole. Thus the effective cross-section for black-hole formation in collisions is decreased. This effect become more severe as  $n_s$  increases because the partons are more likely to be

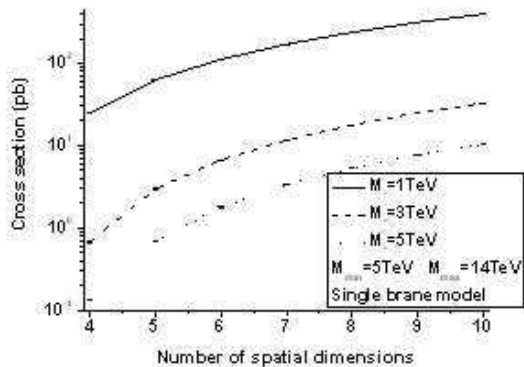


FIG. 7: Cross section for production of a black-hole (rotating or non-rotating) as a function of the number of spatial dimensions, for a tensionless brane, with no fermion brane-splitting.

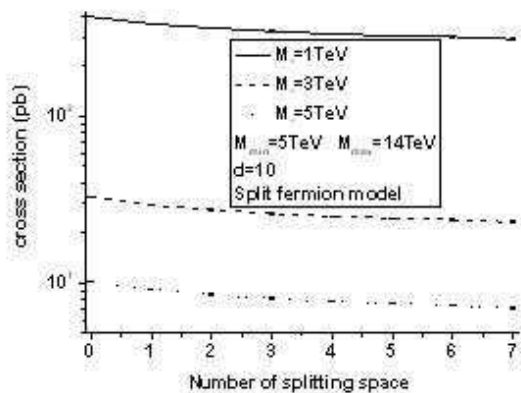


FIG. 9: Cross section for production of a non-rotating black-hole as a function of the number of fermion brane-splitting dimensions for  $d = 10$ .

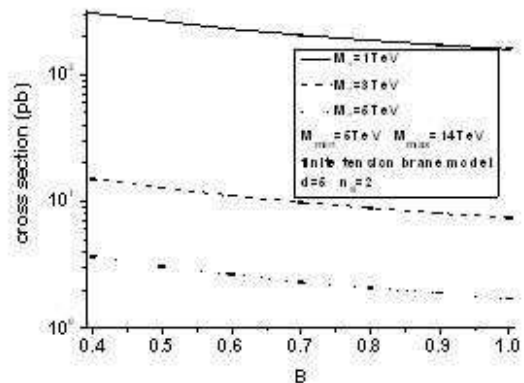


FIG. 8: Cross section for production of a non-rotating black-hole as a function of the deficit angle parameter for  $d = 5$  and  $n_s = 2$ .

more widely separated in the extra dimensions, therefore the cross section decreases with increasing  $n_s$ .

Figure 10 shows the cross section as a function of the chosen minimum black-hole mass. The parton distribution functions strongly suppress the events with high black-hole masses.

Figure 11 shows the cross section for the two-body final-state scenario as a function of the number of spatial dimensions, for  $M_{min} = M_* = 1$  TeV,  $M_{min} = M_* = 3$  TeV and  $M_{min} = M_* = 5$  TeV. It increases with the number of spatial dimensions.

### A. Black-Hole Formation in BlackMax

Within BlackMax, the probability of creating a black-hole of center-of-mass energy  $\sqrt{us}$ , in the collision of two

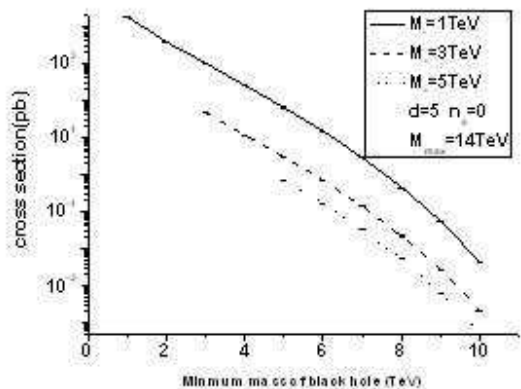


FIG. 10: Cross section for formation of a black-hole (rotating or non-rotating) as function of the minimum mass of black-hole, for a zero-tension brane, with no fermion brane-splitting. The vertical lines are the error bars.

protons of center-of-mass-energy  $\sqrt{s}$ , is given by

$$P(Q') = \int_u^1 \frac{dv}{v} \sum_{ij} f_i(v, Q') f_j\left(\frac{u}{v}, Q'\right). \quad (27)$$

According to the theory, there will be some minimum mass for a black-hole. We expect  $M_{min} \sim M_*$ , but leave  $M_{min} \geq M_*$  as a free parameter. Therefore, a black-hole will only form if  $u > (M_{min}/Q)^2$ . The type of partons from which a black-hole is formed determines the gauge charges of the black-hole. Clearly, the probability to create a black-hole in the collision of any two particular partons  $i$  and  $j$  with energies (momenta)  $vE$  and  $\frac{uE}{v}$ , is given by

$$P(vE, \frac{uE}{v}, i, j) = f_i(v, Q') f_j(u/v, Q') \quad (28)$$

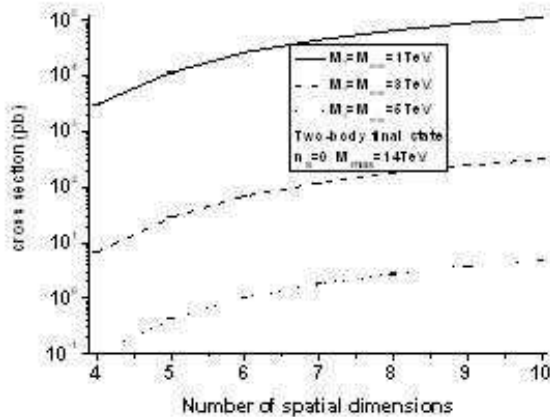


FIG. 11: Cross section for the two-body final-state scenario as a function of number of spatial dimensions where  $M_{min} = M_* = 1$  TeV,  $M_{min} = M_* = 3$  TeV and  $M_{min} = 5$  TeV.

The energies and types of the two colliding partons determine their momenta and affect their locations within the ordinary and extra dimensions. For protons moving in the  $z$ -direction, we arbitrarily put one of the partons at the origin and locate the second parton randomly within a disk in the  $xy$ -plane of radius  $b_{max}(E_{CM} = \sqrt{us}; d)$ .

We must, however, also take into account that the partons will be separated in the extra dimensions as well. Each parton type is given a wave function in the extra dimension. For fermions, these wave functions are parametrized by their centers and widths which are input parameters (cf. Fig 14). In the split-fermion case, the centers of these wave functions may be widely separated; but even in the non-split case, the wave functions have non-zero widths. For gauge bosons, the wave functions are taken to be constant across the (thick) brane.

The output from the generator (described in greater detail below) includes the energies, momenta, and types of partons that yielded black-holes. The locations in time and space of the black-holes are also output.

The formation of the black-hole is a very non-linear and complicated process. We assume that, before settling down to a stationary phase, a black-hole loses some fraction of its energy, linear and angular momentum. We parameterize these losses by three parameters:  $1 - f_E$ ,  $1 - f_P$  and  $1 - f_L$ . Thus the black-hole initial state that we actually evolve is characterized by

$$\begin{aligned} E &= E_{in} f_E; \\ P_z &= P_{zin} f_P; \\ J' &= L_{in} f_L; \end{aligned} \quad (29)$$

where  $E_{in}$ ,  $P_{zin}$  and  $L_{in}$  are initial energy, momentum and angular momentum of colliding partons, while  $f_E$ ,  $f_P$  and  $f_L$  are the fractions of the initial energy, momentum

and angular momentum that are retained by the stationary black-hole. We expect that most of the energy lost in the non-linear regime is radiated in the form of gravitational waves and thus represents missing energy. Yoshino and Rychkov [46] have calculated the energy losses by numerical simulation of collisions. Their results will be incorporated in a future upgrade of BlackMax.

For a small black-hole, the numerical value for the angular momentum is of the order of several  $\hbar$ . In that range of values, angular momentum is quantized. Therefore a black-hole cannot have arbitrary values of angular momentum. We keep the actual angular momentum of the black-hole,  $J$ , to be the nearest half-integer, i.e.  $2J = [2J' + \frac{1}{2}]$ .

The loss of the initial angular momentum in the non-linear regime has as a consequence that the black-hole angular momentum is no longer in the transverse plane of the colliding protons. We therefore introduce a tilt in the angular-momentum

$$\theta \equiv \cos^{-1}\left(\frac{J}{\sqrt{J(J+1)}}\right). \quad (30)$$

Figure 12 illustrates this geometry.

In this version of the generator, we have assumed that the angular-momentum quantum numbers of the black-hole were  $(J, J_m = J)^4$ . We next randomly choose an angle  $\phi$ , and then reset the angular-momentum axis to  $(\theta, \phi)$ .

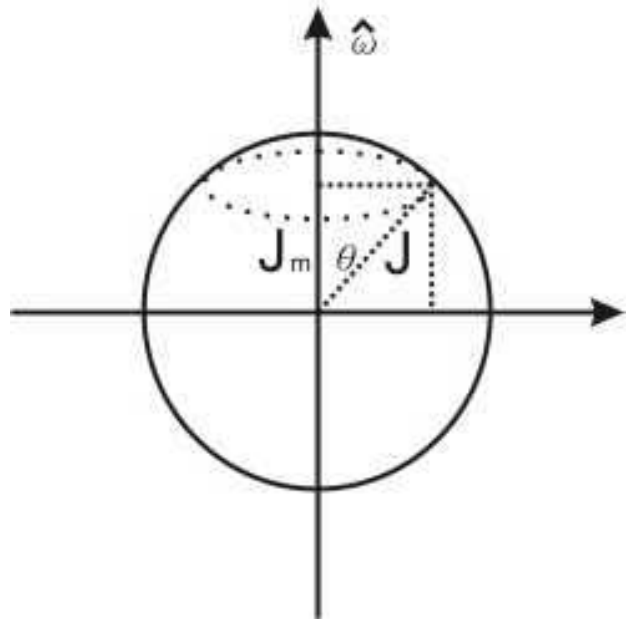


FIG. 12: Angular momentum tilt geometry.

<sup>4</sup> Future versions of the generator may randomize the choice of  $J_m$ .

### III. GRAY-BODY FACTORS

Once the black-hole settles down to its stationary configuration, it is expected to emit semi-classical Hawking radiation. The emission spectra of different particles from a given black-hole depend in principle on the mass, spin and charge of the black-hole, on the “environment”<sup>5</sup> and on the mass and spin of the particular particle. Wherever possible we have made use of the correct emission spectrum often phrased in terms of the gray-body factor for black-holes in 3+1-dimensional space-time. In most cases, these were extant in the literature, but we have calculated the spectra for the split-fermion model ourselves, and reproduced existing spectra independently. The sources of the gray-body factors are summarized in Table I.

- *Non-rotating black-hole on a tensionless brane:* For a non-rotating black-hole, we used previously known gray-body factors for spin 0, 1/2 and 1 fields in the brane, and for spin 2 fields (*i.e.* gravitons) in the bulk.
- *Rotating black-hole on a tensionless brane:* For rotating black-holes, we used known gray-body factors for spin 0, 1/2 and 1 fields on the brane. The correct emission spectrum for spin 2 bulk fields is not yet known for rotating black-holes, we currently do not allow for the emission of bulk gravitons from rotating black-holes. *As discussed below, this remains a serious shortcoming of current micro-black-hole phenomenology, since super-radiance might be expected to significantly increase graviton emission from rotating black-holes, and thus increase the missing energy in a detector.*
- *Non-rotating black-holes on a tensionless brane with fermion brane splitting:* In the split-fermion models, gauge fields can propagate through the bulk as well as on the brane, so we have calculated gray-body factors for spin 0 and 1 fields propagating through the bulk, but only for a non-rotating black-hole for the split-fermion model. These are shown in Figures 50-61.
- *Non-rotating black-holes on a non-zero tension brane:* The bulk gray-body factors for a brane with non-zero tension are affected by non-zero tension because of the modified bulk geometry (deficit angle). We have calculated gray-body factors for spin 0, 1 and 2 fields propagating through the bulk,

again only for the non-rotating black-hole for a brane with non-zero tension and  $d = 5$ .

- *Two particle final states:* We use the same gray-body factors as a non-rotating black-hole to calculate the cross section of two-particle final states (excluding gravitons).

In all cases, the relevant emission spectra are loaded into a data base as described in appendices A.

### IV. BLACK-HOLE EVOLUTION

The Hawking radiation spectra are calculated for the black-hole at rest in the center-of-mass frame of the colliding partons. The spectra are then transformed to the laboratory frame as needed. In all cases we have not (yet) taken the charge of the black-hole into account in calculating the emission spectrum, but have included phenomenological factors to account for it as explained below.

The degrees of freedom of the Standard-Model particles are given in Table II. Using the calculated Hawking spectrum and the number of degrees of freedom per particle, we determine the expected radiated flux of each type of particle as a function of black-hole and environmental properties. For each particle type  $i$  we assign to it a specific energy,  $\hbar\omega_i$  with a probability determined by that particle’s emission spectrum. (The particle “types” are listed in Table II.)

Assume a black-hole with mass  $M_{bh}$  emits a massless particle with energy  $\hbar\omega_i$ . The remaining black-hole will have energy and momentum like

$$(M_{bh} - \hbar\omega_i, -\hbar\omega_i) \quad (31)$$

Here we ignore the other dimensions. We use a classical model to simulate the events. The mass of the remaining black-hole should remain positive. So from equation (31) one gets

$$\hbar\omega_i < M_{bh}/2. \quad (32)$$

Combining this with the observation that energy of a particle is larger than its mass, leads us to require that

$$M_i < \hbar\omega_i \quad (33)$$

We next need to determine whether that particle with that energy is actually emitted within one generator time-step  $\Delta t$ . The time-step itself is an input parameter (cf. figure 14). We choose a random number  $N_r$  from the interval  $[0, 1]$ . Given  $L_{Fi}$ , the total number flux of particles of type  $i$ , and  $N_i$ , the number of degrees of freedom of that particle type, the particle will be emitted if

$$L_{Fi}N_i\Delta t > N_r. \quad (34)$$

---

<sup>5</sup> dimensionality and geometry of the bulk, brane tension, location of fermionic branes



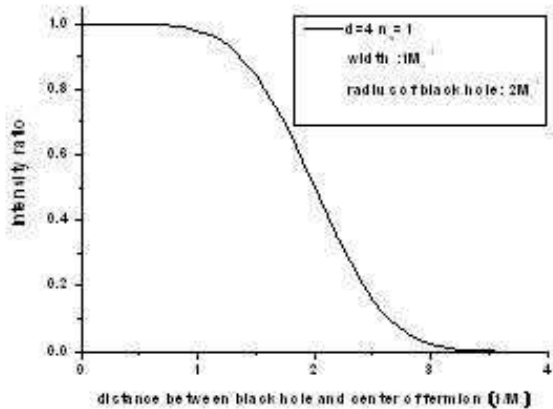


FIG. 13: The emitted fermion intensity (normalized to one) as a function of the distance between the black-hole and the center of the gaussian distribution of a fermionic brane. As a black-hole increases the distance from a fermionic brane due to recoil the intensity of the emitted fermions of that type falls down quickly. The radius of black-hole is set to be  $2M_*^{-1}$ . The width of the fermionic brane is  $M_*^{-1}$ . The plot is for the case of one extra dimension.

In the single-brane model,  $L_{Fi}$  is derived from the power spectrum of the Hawking radiation. In the split-fermion model, we include a suppression factor for fermions. The factor depends on the overlap between the particular fermion brane and the black-hole when the black-hole is not located on that fermion's brane. Fig. 13 shows how the spectrum of emitted particles changes as the black-hole drifts away from the center of the fermion brane. As a black-hole increases its distance from a fermion brane due to recoil, the intensity of the emitted fermions of that type declines quickly.

If the particle is to be emitted, we choose its angular-momentum quantum numbers  $(l, m)$  according to:

$$P_{em}(i, l, m, E) = L_{i,l,m}(E) / \sum_{l',m'} L_{i,l',m'}(E). \quad (35)$$

Here  $P_{em}(i, l, m, E)$  is the probability that a type  $i$  particle with quantum numbers  $(l, m)$  will be emitted.  $L_{i,l,m}(E)$  is the emission spectrum of a particle of type  $i$  with quantum numbers  $(l, m)$ . This step is omitted in the case of non-rotating black-holes since we do not follow the angular-momentum evolution of the black-hole.

Once the quantum numbers of the emitted particle are determined, we calculate the direction of emission according to the corresponding spheroidal wave function:

$$P_{em}(\theta, \phi) = |\Psi_{lm}(\theta, \phi)|^2 \sin \theta \Delta \theta \Delta \phi \quad (36)$$

Here  $P_{em}(\theta, \phi)$  is the probability of emission in the  $(\theta, \phi)$  direction for the angular quantum numbers  $(l, m)$ .  $\Psi_{lm}(\theta, \phi)$  is the (properly normalized) spheroidal wave

function of the mode with those angular quantum numbers.

Once the energy and angular-momentum quantum numbers are determined for the  $i$ -th particle type, then, if that particle type carries SU(3) color we assign the color randomly. The color is treated as a three-dimensional vector  $\vec{c}_i = (r, b, g)$ , in which a quark's color-vector is either  $(1, 0, 0)$ ,  $(0, 1, 0)$ , or  $(0, 0, 1)$ . Similarly, an anti-quark has  $-1$  entries in its color-vector. A gluon's color-vector has one  $+1$  entry, and one  $-1$  entry.

The black-hole gray-body factors which quantify the relative emission probabilities of particles with different spin are calculated for a fixed background, i.e. assuming that the black-hole metric does not change during the emission process. However, as the black-hole emits particles, the spin and charge of the black-hole do change.

### A. Electric and Color Charge Suppression

A charged and highly rotating black-hole will tend to shed its charge and angular momentum. Thus, emission of particles with charges of the same sign as that of the black-hole and angular momentum parallel to the black-hole's will be preferred. Emission of particles that increase the black-hole's charge or angular momentum should be suppressed. The precise calculation of these effects has not as yet been accomplished. Therefore, to account for these effects we allow optional phenomenological suppression factors for both charge and angular momentum.

The following charge-suppression factors can currently be used by setting parameter 19 (cf. section VI) equal to 2.

$$F^Q = \exp(\zeta_Q Q^{bh} Q^{em}) \quad (37)$$

$$F_a^3 = \exp(\zeta_3 c_a^{bh} c_a^{em}) \quad a = r, b, g. \quad (38)$$

$Q^{bh}$  is the electromagnetic charge of the black-hole,  $Q^{em}$  is the charge of the emitted particle;  $c_a^{bh}$ , is the color value for the color  $a$ , with  $a = r, b, g$ , of the black-hole, and  $c_a^{em}$ , is the color value for the color  $a$ , with  $a = r, b, g$ , of the emitted particle.  $\zeta_Q$  and  $\zeta_3$  are phenomenological suppression parameters that are set as input parameters of the generator.

We estimate  $\zeta_Q = \mathcal{O}(\alpha_{em})$  and  $\zeta_3 = \mathcal{O}(\alpha_s)$ , where  $\alpha_{em}$  and  $\alpha_s$  are the values of the electromagnetic and strong couplings at the Hawking temperature of the black-hole. Note that we currently neglect the possible restoration of the electroweak symmetry in the vicinity of the black-hole when its Hawking temperature is above the electroweak scale. Clearly, since  $\alpha_{em} \simeq 10^{-2}$  we do not expect electromagnetic (or more correctly) electroweak charge suppression to be a significant effect. However, since  $\alpha_s(1 \text{ TeV}) \simeq 0.1$ , color suppression may well play a role in the evolution of the black-hole.

Once we have determined the type of particle to be emitted by the black-hole, we draw a random number  $N_r$  between 0 and 1 from a uniform distribution. If  $N_r > F^Q$  then the emission process is allowed to occur, if  $N_r < F^Q$  then the emission process is aborted. We repeat the same procedure for color suppression factor,  $F_a^3$ . Thus, particle emission which decreases the magnitude of the charge or color of the black-hole is unsuppressed; this suppression prevents the black-hole from acquiring a large charge/color, and gives preference to particle emission which reduces the charge/color of the black-hole.

### B. Movement of the Black-Hole during Evaporation

We choose the direction of the momentum of the emitted particle ( $\vec{P}_e$ ) according to equation (36) in the center-of-mass frame and then transform the energy and momentum to their laboratory frame values  $\hbar\omega'$  and  $\vec{P}'_e$ . The black-hole properties (energy, momentum, mass, colors, and charge) are then accordingly updated for the next time step:

$$E(t + \Delta t) = E(t) - \hbar\omega' \quad (39)$$

$$\vec{P}(t + \Delta t) = \vec{P}(t) - \vec{P}'_e \quad (40)$$

$$M(t + \Delta t) = \sqrt{E(t + \Delta t)^2 - \vec{P}(t + \Delta t)^2} \quad (41)$$

$$\vec{c}^{bh}(t + \Delta t) = \vec{c}^{bh}(t) - c_i \quad (42)$$

$$Q^{bh}(t + \Delta t) = Q^{bh}(t) - Q_i \quad (43)$$

Here  $\vec{c}^{bh}$  is the color 3-vector of the black-hole and can have arbitrary integer entries.

Due to the recoil from the emitted particle, the black-hole will acquire a velocity  $\vec{v}$  and move to a position  $\vec{x}$ :

$$\vec{v}(t) = \vec{P}(t)/E \quad (44)$$

$$\vec{x}(t + \Delta t) = \vec{x}(t) + \vec{v}(t)\Delta t \quad (45)$$

Since fermions are constrained to live on the 3+1-dimensional regular brane, the recoil from fermions is not important. Only the emission of vector fields, scalar fields and gravitons gives a black hole momentum in extradimension. Once a black hole gains momentum in extradimension, it is able to leave the regular brane if it carries no gauge charge. In the split fermion case, it can move within the mini-bulk even if it carries gauge charge. In the case of rotating black holes, because the gray-body factor for gravitons is not yet known, graviton emission is turned off in the generator and the black holes experience no bulk recoil.

Recoil can in principle change the radiation spectrum of the black-hole in two ways. First, the spectrum will not be perfectly thermal or spherically symmetric in the laboratory frame, but rather boosted due to the motion

of the black-hole. However, as we shall see, the black-hole never becomes highly relativistic, so the recoil does not significantly affect the shape of the spectrum.

As the lifetime of a small black-hole is relatively short, and its recoil velocity non-relativistic, it does not move far from its point of creation. However, even a recoil of the order of one fundamental length  $\sim M_*^{-1}$  in the bulk direction could dislocate the black-hole from the brane<sup>6</sup>. In single-brane models this would result in apparent missing energy for an observer located on the brane able to detect only Standard Model particles. In the split-fermion model, as the black-hole moves off or on particular fermion branes, the decay channels open to it will change.

### C. Rotation

Since two colliding particles always define a single plane of rotation, rotating black-holes are formed with a single rotational parameter. For two particles colliding along the  $z$ -axis, there should be only one rotation axis perpendicular to the  $z$ -axis. However, due to angular-momentum loss both in the formation process, and subsequently in the black-hole decay, three things can happen: i) the amount of rotation can change, ii) the rotation axis can be altered, and iii) more rotation axes can emerge, because there are more than three spatial dimensions. Also, if the colliding particles have a non-zero impact parameter in bulk directions<sup>7</sup> the plane of rotation will not lie entirely in the brane direction. Because solutions do not exist for rotating black-holes with more than one rotation axis, we forbid the emergence of secondary rotation axes. We do, on the other hand, allow the single rotation axis of the black-hole to evolve. However, no gray-body factors are known if the single rotation axis acquires components in the extra dimensions, therefore we limit the rotation axis to the brane dimensions. Relaxing these limitations is a subject for future research.

We next must determine the rotational axis of the black-hole. The rotation parameter of a black-hole with angular-momentum quantum numbers  $(j, j)$  is taken to be

$$a = \frac{J}{M} \frac{n+2}{2}, \quad (46)$$

where  $J = \sqrt{j(j+1)}\hbar$ . The direction of the black-hole angular momentum is taken to be

$$\vec{J} = j\hbar\hat{\omega} + \sqrt{j}\hbar\hat{l}_\perp, \quad (47)$$

<sup>6</sup> This is very unlikely because most of the black-holes have gauge charges.

<sup>7</sup> Due to the finite thickness of the single brane or splitting between the quark branes.

where  $\hat{l}_\perp$  is a unit vector in the plane perpendicular to  $\hat{\omega}$ . We chose the direction of  $\hat{l}_\perp$  randomly.

When the black-hole emits a particle with angular-momentum quantum numbers  $(l, m)$ , there are several possible final states in which the black-hole can end up. We use Clebsch-Gordan coefficients to find the probability of each state.

$$|j, j\rangle = \sum_{j' \leq j+l}^{j-l} C(j, j; l, m, j', j-m) |l, m\rangle |j', j-m\rangle \quad (48)$$

We use  $|C(j, j; l, m, j', j-m)|^2$  as the probability that the new angular-momentum quantum numbers of the black-hole will be  $(j', j-m)$ . From angular-momentum conservation  $\vec{J} = \vec{L} + \vec{J}'$ , we can calculate the tilt angle of the black-hole rotation axis as:

$$\cos\theta = \frac{j(j+1) + j'(j'+1) - l(l+1)}{2\sqrt{j(j+1)j'(j'+1)}}. \quad (49)$$

We randomly choose a direction with the tilt angle  $\theta$  as a new rotation axis and change quantum numbers to  $(j', j')$ .

In calculating the gray-body factors, the black hole is always treated as a fixed unchanging background. The power spectrum of emitted particles can be calculated from

$$\frac{dE}{dt} = \sum_{l,m} |A_{l,m}|^2 \frac{\omega}{\exp((\omega - m\Omega)/T_H) \mp 1} \frac{d\omega}{2\pi}. \quad (50)$$

Here  $l$  and  $m$  are angular momentum quantum numbers.  $\omega$  is the energy of the emitted particle.  $\Omega$  is defined by

$$\Omega = \frac{a_*}{(1 + a_*^2)r_h}. \quad (51)$$

The exponential factor in the denominator of (50) causes the black hole to prefer to emit high angular momentum particles. However, since the TeV black holes are quantum black holes, the gray-body factors should really depend on both the initial and final black-hole parameters. The calculation of the gray-body spectra on a fixed background can cause some problems. In particular, in the current case, the angular momentum of the emitted particle (as indeed the energy) may well be comparable to that of the black hole itself. There should be a suppression of particle emission processes in which the black hole final state is very different from the initial state. We therefore introduce a new phenomenological suppression factor, parameter 17, to reduce the probability of emission events in which the angular momentum of the black hole changes by a large amount.

If parameter 17 is equal to 1 (cf. section VI), we do not take into account the suppression of decays which increase the angular momentum of the black-hole. If we

are using  $\Delta$ Area suppression (parameter 17 equal to 2) then

$$F^L = \exp(\zeta_L(r_h^{bh}(t + \Delta t)^2/r_h^{bh}(t)^2 - 1)). \quad (52)$$

If we are using  $J_{bh}$  suppression (parameter 17 equal to 3) then

$$F^L = \exp(-\zeta_L |J^{bh}(t + \Delta t)|). \quad (53)$$

If we are using  $\Delta J_{bh}$  suppression (parameter 17 equal to 4) then

$$F^L = \exp(-\zeta_L |J^{bh}(t + \Delta t) - J^{bh}(t)|). \quad (54)$$

We might expect  $\zeta_L \sim 1$ , however there is no detailed theory to support this; as indeed there is no detailed theory to choose among these three phenomenological suppression factors. It is also worth noting that, while for  $d = 3$  and  $d = 4$  there is a maximum angular momentum that a black-hole of a given mass can carry, for  $d \geq 5$  there is no such upper limit. We do impose that  $a \leq R_s/2$  for  $d = 3$  and  $a \leq R_s$  for  $d = 4$ .

As for the charge and color suppression, we choose a random number  $N_r$  between 0 and 1. If  $N_r > F^L$  then the particle emission is aborted.

The procedure described in this section is then repeated at each time step with each particle type, and then successive time steps are taken until the mass of the black-hole falls below  $M_*$ . In practice, the time step should be set short enough that in a given time step the probability that particles of more than one type are emitted is small. We set the time step to  $\Delta t = 10^{-5} \text{ GeV}^{-1}$ .

In two-body final states, one expects no black-hole, and hence no black-hole decay by emission of Hawking radiation. The generator therefore proceeds directly to the final burst phase.

## V. FINAL BURST

In the absence of a self-consistent theory of quantum gravity, the last stage of the evaporation cannot be described accurately. Once the mass of black-hole becomes close to the fundamental scale  $M_*$ , the classical black-hole solution can certainly not be used anymore. We adopt a scenario in which the final stage of evaporation is a burst of particles which conserves energy, momentum and all of the gauge quantum numbers. For definiteness, we assume the remaining black-hole will decay into the lowest number of Standard-Model particles that conserve all quantum number, momentum and energy.

A black-hole with electromagnetic charge  $Q^{bh}$  and color-vector  $\vec{c}^{bh} = (r^{bh}, b^{bh}, g^{bh})$  will be taken to emit  $N_{-1/3}$  down-type quarks (i.e. d,s or b quarks),  $N_{2/3}$  up-type quarks (u,c, or t),  $N_{-1}$  charged leptons and  $W$

bosons,  $N_{gl}$  gluons, and  $N_n$  non-charge particles (ie.  $\gamma$ ,  $Z$  and Higgs). We use the following procedure to determine  $\vec{N}_{burst} \equiv (N_{-1/3}, N_{2/3}, N_{-1}, N_{gl}, N_n)$ .

Step 1: preliminary solution:

- Search all possible solutions with  $N_n = 0$ .
- Choose the minimum number of particles as preliminary solution.

Step 2: Actual charged/colored emitted particle count:

- The preliminary  $\vec{N}_{burst} \equiv (N_{-1/3}, N_{2/3}, N_{-1}, N_{gl}, N_n)$  having now been determined. If the minimum number of solution is less than 2, we then add  $N_n$  to keep the total number equal to 2. Later we choose one of them randomly according to the degrees of freedom of each particle.
- After obtaining the number of emitted particles, we randomly assign their energies and momenta, subject to the constraint that the total energy and momentum equal that of the final black-hole state. We currently neglect any bulk components of the final black-hole momentum.

## VI. INPUT AND OUTPUT

The input parameters for the generator are read from the file parameter.txt, see Fig.14:

1. **Number\_of\_simulations**: sets the total number of black-hole events to be simulated;
2. **Center\_of\_mass\_energy\_of\_protons**: sets the center-of-mass energy of the colliding protons in GeV;
3. **M\_ph**: sets the fundamental quantum-gravity scale ( $M_*$ ) in GeV;
4. **Choose\_a\_case**: defines the extra dimension model to be simulated:
  - (a) 1: non-rotating black-holes on a tensionless brane with possibility of fermion splitting,
  - (b) 2: non-rotating black-holes on a brane with non-zero positive tension,
  - (c) 3: rotating black-holes on a tensionless brane with  $d=5$ ,
  - (d) 4: two-particle final-state scenario;
5. **number\_of\_extra\_dimensions**: sets the number of extra dimensions; this must equal 2 for brane with tension (**Choose\_a\_case=2**);

6. **number\_of\_splitting\_dimensions**: sets the number of extra split-fermion dimensions (**Choose\_a\_case=1**);
7. **extradimension\_size**: sets the size of the mini-bulk<sup>8</sup> in units of  $1/\text{TeV}$  (**Choose\_a\_case=1**);
8. **tension**: sets the deficit-angle parameter  $B$  [14, 15] (**Choose\_a\_case=2**);
9. **choose\_a\_pdf\_file**: defines which of the different CTEQ6 parton-distribution functions (PDF) to use;
10. **Minimum\_mass**: sets the minimum mass  $M_{min}$  in GeV of the initial black-holes;
11. **fix\_time\_step**: If equal to 1, then code uses the next parameter to determine the time interval between events; if equal to 2 then code tries to optimize the time step, keeping the probability of emitting a particle in any given time step below 10%.
12. **time\_step**: defines the time interval  $\Delta t$  in  $\text{GeV}^{-1}$  which the generator will use for the black-hole evolution;
13. **Mass\_loss\_factor**: sets the loss factor 0 for the energy of the initial black-hole, as defined in equation 29;
14. **momentum\_loss\_factor**: defines the loss factor  $0 \leq f_p \leq 1$  for the momentum of initial black-holes as defined in equation 29;
15. **Angular\_momentum\_loss\_factor**: sets the loss factor  $0 \leq f_L \leq 1$  for the angular momentum of initial black-holes as defined in equation 29;
16. **Seed**: sets the seed for the random-number generator (9 digit positive integer);
17. **L\_suppression**: chooses the model for suppressing the accumulation of large black-hole angular momenta during the evolution phase of the black-holes (cf. discussion surrounding equations 52-54);
  - 1: no suppression;
  - 2:  $\Delta$  Area suppression;
  - 3:  $J_{bh}$  suppression;
  - 4:  $\Delta J$  suppression;

---

<sup>8</sup> This is the distance between fermion branes where only gauge bosons and Higgs field can propagate in split-fermion brane scenario.



18. **angular\_momentum\_suppression\_factor**: defines the phenomenological angular-momentum suppression factor,  $\zeta_L$  (cf. discussion surrounding equation 52-54);
  19. **charge\_suppression**: turns the suppression of accumulation of large black-hole electromagnetic and color charge during the black-hole evolution process on or off (cf. discussion surrounding equation 37)
    - 0: charge suppression turned off;
    - 1: charge suppression turned on;
  20. **charge\_suppression\_factor**: sets the electromagnetic charge suppression factor,  $\zeta_Q$ , in 37;
  21. **color\_suppression\_factor**: sets the color charge suppression factor,  $\zeta_3$  in 37;
- 21-94 (odd entries:) the widths of fermion wave functions (in  $M_*^{-1}$  units); and (even entries:) centers of fermion wave functions (in  $M_*^{-1}$  units) in split-brane models, represented as 9-dimensional vectors (for non-split models, set all entries to 0).
- When the code terminates, the file output.txt with all the relevant information (i.e. input parameters, cross section) is output to the working directory. This file contains also different segments of information about the generation of black-holes which are labelled at the beginning of each line with an ID word (Parent, Pbh, trace, Pem, Pemc or Elast):
- **Parent**: identifies the partons whose collision resulted in the formation of the initial black-hole (see Fig. 16).
    - column 1: identifies the black-hole;
    - column 2: PDGID code of the parton;
    - column 3: energy of the parton;
    - columns 4-6: brane momenta of the parton.
  - **Pbh**: contains the evolution of the charge, color, momentum and energy of the black-holes, and, for rotating black-holes, their angular momentum (cf. Fig. 17).
    - column 1: identifies the black-hole;
    - column 2: time at which the black-hole emitted a particle;
    - column 3: PDGID code of a black-hole;
    - column 4: three times the electromagnetic charge of the black-hole;
    - columns 5 to 7: color-charge vector components of the black-hole;
  - columns 8: energy of the black-hole in the laboratory frame;
  - columns 9 to 11: brane components of the black-hole momentum in the laboratory frame;
  - columns 12 to (8+d): bulk components of the black-hole momentum;
  - column (9+d): angular momentum of the black-hole, in the case of rotating black-holes; empty otherwise.
  - **trace**: contains the evolution history of the black-holes' positions (cf. Fig. 18):
    - column 1: identifies the black-hole;
    - column 2: the times at which the black-hole emitted a particle;
    - columns 3 to 5 are the brane components of the black-hole position vector when the black-hole emitted a particle;
    - columns 6 to (2+d): the bulk components of the black-hole position vector, when the black-hole emitted a particle.
  - **Pem**: contains a list of the black-holes, with the history of their evolution (cf. Fig. 19):
    - column 1: identifies the black-hole;
    - column 2: the times at which the black-hole emitted a particle;
    - column 3: PDGID code of the emitted particle;
    - column 4: three times the charge of the emitted particle;
    - columns 5 to 7: color-vector components of the emitted particle;
    - columns 8: energy of the emitted particle in the laboratory frame;
    - columns 9 to 11: brane components of the momentum of the emitted particle, in the laboratory frame;
    - columns 12 to (8+d): bulk components of the momentum of the emitted particle.
  - **Pemc**: contains the same information as Pem, but in the center-of-mass frame of the collision.
  - **Elast**: contains the same information as Pem for the particles emitted in the final decay burst of the black-hole. Column 12 and onwards are omitted as these particles have no bulk momentum.

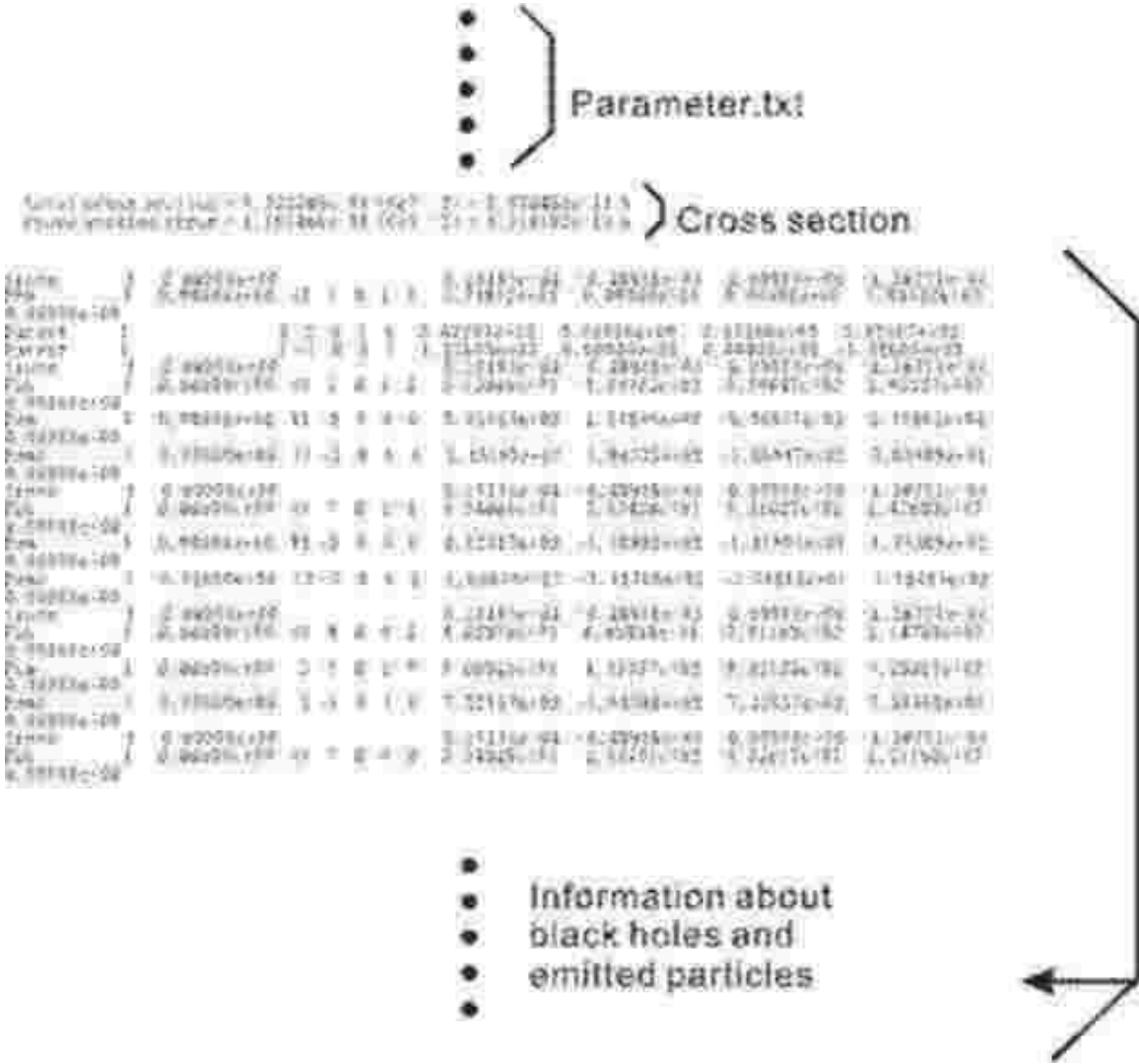


FIG. 15: Output.txt: There are three parts to this file. The first part is a copy of parameter.txt. The second part includes information about the black-hole and the emitted particles. The first column identifies the what type of information each row is supplying – parent is information about the two incoming partons; Pbh is information on the energy and momenta of the produced black-holes; trace describes the location of the black-holes; Pem characterizes the emitted particles in the lab frame; Pcmc characterizes the emitted particles in the center-of-mass frame; Elast describes the final burst. The third part of the file is the black-hole production cross-section as inferred from the events in this generator run.

**VII. RESULTS**

We choose the following parameters for the distributions shown in this section and normalize them to an integrated luminosity of  $10 fb^{-1}$ , unless otherwise stated. The values of the parameters are chosen to be the same as in figure 14, except where a parameter is varied to study its effect.

- Number\_of\_simulations = 10000;
- Center\_of\_mass\_energy\_of\_protons = 14000 GeV;
- M\_ph = 1000 GeV;
- extradimension\_size = 10 TeV<sup>-1</sup>;
- choose\_a\_pdf\_file=0;
- Minimum\_mass=5000 GeV;
- time\_step=10<sup>-5</sup> GeV<sup>-1</sup>;
- Mass\_loss\_factor=0.0;
- momentum\_loss\_factor=0.0;
- Angular\_momentum\_loss\_factor=0.2;
- Seed=123589341;
- L\_suppression=1;

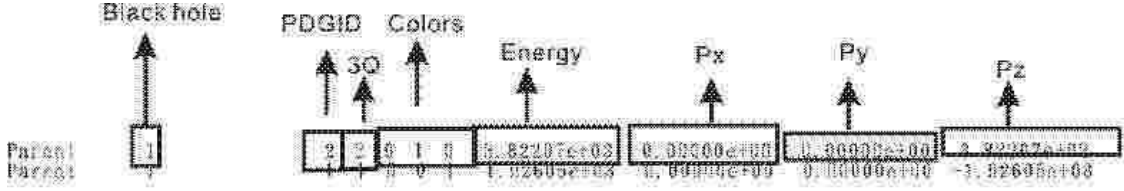


FIG. 16: Lines in the output file headed by the ID = Parent contain information about the initial partons which formed the black-hole.

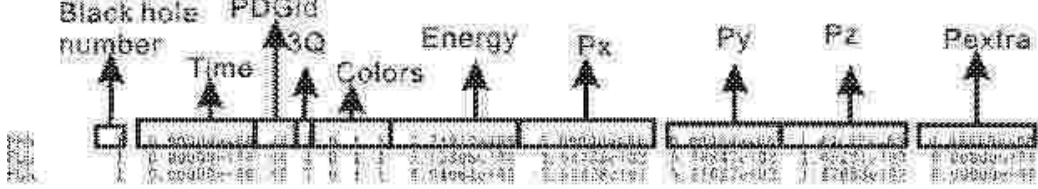


FIG. 17: Lines in the output file headed by the ID = Pbh contain the energies and momenta of the black-holes for each emission step. In case of rotating black-holes, the last column in the line is the angular momentum.

- charge\_suppression=1;
- charge\_suppression\_factor irrelevant since charge\_suppression=1;
- color\_suppression\_factor irrelevant since charge\_suppression=1;
- widths of fermion wave functions =  $1 M_*^{-1}$  ;
- centers of quark wave functions:  $(10^{-2}/3, 0, 0, \dots)(\text{GeV}^{-1})$  (i.e. all quarks have Gaussian wave functions centered on a point displaced from the origin by  $10^{-2}/3\text{GeV}^{-1}$  in the first splitting direction);
- distribution center of leptons:  $(-10^{-2}/3, 0, 0, \dots)(\text{GeV}^{-1})$ .

In this section, we present some distributions of properties of the initial and evolving black-holes and of the particles which are emitted by them during the Hawking radiation and final-burst phases.

#### A. Mass of the Initial Black-Holes

Figures 21, 22 and 23 show the the initial black-hole mass distribution for three different extra dimension scenarios: non-rotating black-holes on a tensionless brane, non-rotating black-holes on a non-zero tension brane and non-rotating black-holes with split fermion branes respectively. Because we chose 5 TeV as the minimum mass of the initial black-hole, the distributions have a cut off at 5 TeV.

#### B. Movement of Black-Holes in the Bulk

The generator includes recoil of black-holes due to Hawking radiation. The recoil modifies the spectrum due to the Doppler effect. Even if the effect is small, the high energy tail of the emitted particle's energy spectrum is longer than for pure Hawking radiation. Fig. 24 shows the random motion in the mini-bulk for 10,000 black-holes as consequence of recoil. While most of the black-holes remain on the brane where they were formed, a significant number of them are capable of drifting all the way to the lepton brane. There are also a few events where the black holes leave the mini-bulk completely. Since Standard-Model charges are confined to the mini-bulk, a black-hole needs to carry zero charge in order to be able to leave the mini-bulk. Once out of the mini-bulk, a black-hole cannot emit Standard-Model particles anymore. Models with an additional bulk  $Z_2$  symmetry (e.g. Randall Sundrum models) do not allow for a black-hole recoil from the brane [27]. Unfortunately, the number of black-holes which escape the mini-bulk is so small that experimentally we are unlikely to be able to distinguish between models on this basis.

#### C. Initial Black-Hole Charge Distribution

Most of the initial black-holes are created by u and d quarks. Denote by  $N_{3Q}$  the number of black-holes that have electromagnetic charge  $Q$ . Fig. 25 is a histogram of  $3Q$  for  $n_s = 0$ ,  $n_s = 4$ , and  $n_s = 7$  in  $d = 10$  space. Since at these parton momenta, there are roughly twice as many u-quarks in a proton as d-quarks, we expect that most of the black-holes have  $3Q = 4$ . i.e. are made of two



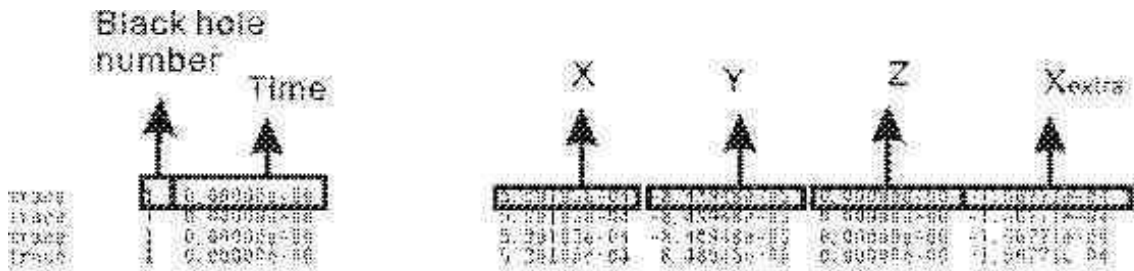


FIG. 18: Lines in the output file headed by the ID = trace contain the location of the black-hole for each emission step.

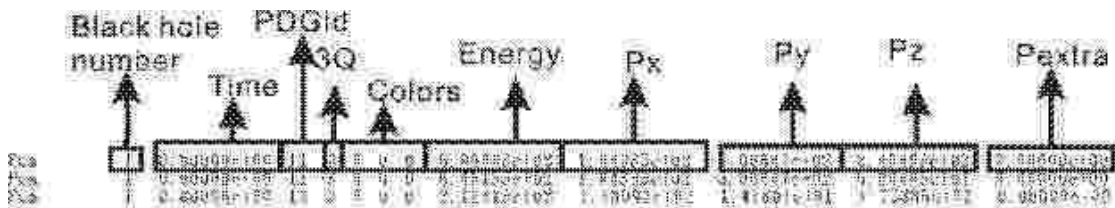


FIG. 19: Lines in the output file headed by the ID = Pem contain the types of the emitted particles, their energies and momenta in the lab frame and the times of their emission.

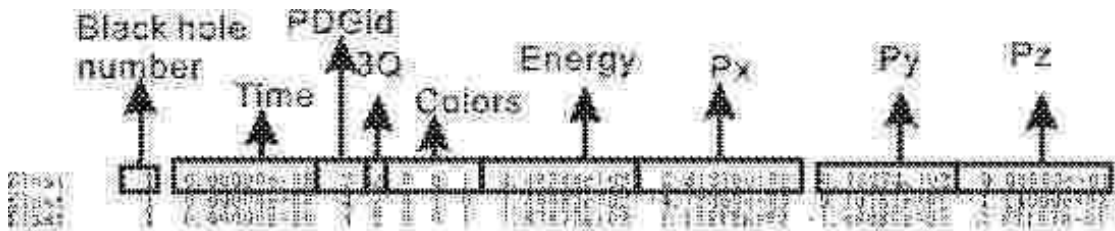


FIG. 20: Lines in the output file headed by the ID = Elast contain the types, energies and momenta of particles of the final burst.

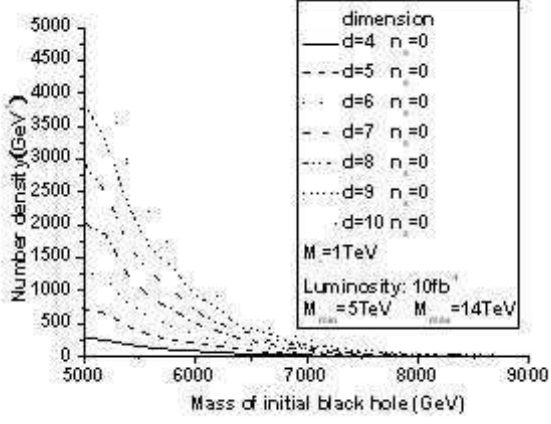


FIG. 21: Mass distribution of initial black-holes (rotating and non-rotating) on a tensionless brane for various numbers of extra dimension.

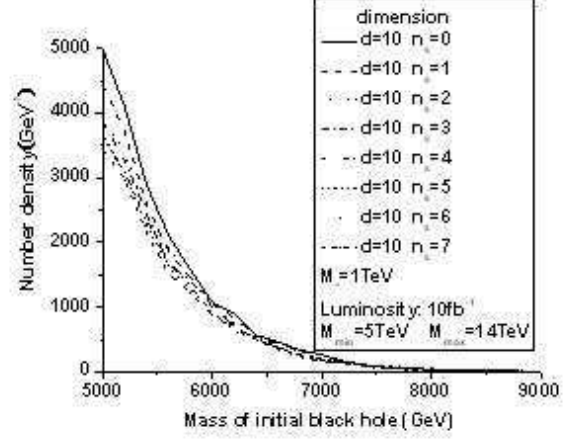


FIG. 23: Mass distribution of initial (non-rotating) black-holes on a tensionless brane for  $d = 10$  and different numbers of split-fermion branes.

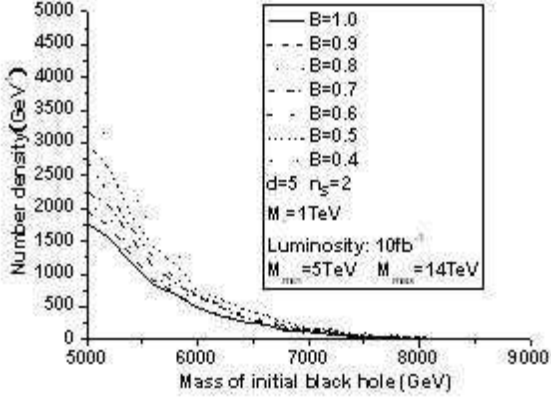


FIG. 22: Mass distribution of initial (non-rotating) black-holes on a non-zero tension brane for  $B = 1.0$ ,  $B = 0.8$  and  $B = 0.6$ .

u-quarks ( $f_{uu}$ ). One does indeed see a large peak at  $3Q = 4$  in figure 25. A second peak at  $3Q = 1$  corresponds to black-holes made of one d and one u-quark, or from one anti-d and one gluon. Since there are only a few gluons or anti-quarks at these momenta,  $f_1 \simeq f_{ud}$ .

Similarly, the small peak at  $3Q = -2$  is predominantly  $dd$  and not  $\bar{u}$ -gluon.

We expect that  $f_{ud} \simeq 2\sqrt{f_{uu}f_{dd}}$ , and thus  $f_1 \simeq 2\sqrt{f_4f_{-2}}$ . This relation is roughly satisfied in Fig. 25. In the split-fermion case, since gluons can move in the mini-bulk, there is a further suppression of the gluon contribution due to the wave-function-overlap suppression between the gluons and fermions. In particular  $3Q = 2$  and  $3Q = -1$ , which are dominated by gluon-quark collisions, are suppressed, as can be seen in Fig.25. For a large number of split dimensions, there are almost no

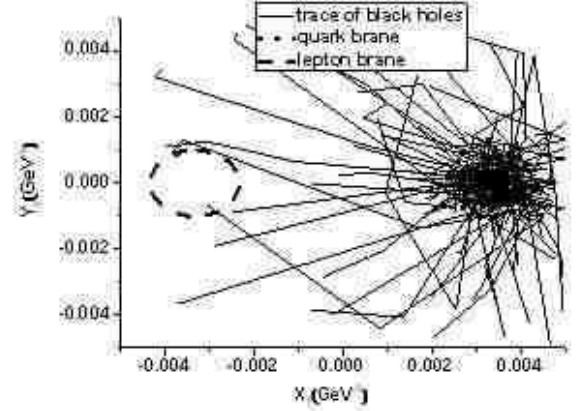


FIG. 24: black-hole movement in the mini-bulk due to recoil.  $X_1, Y_1$  are coordinates in two extra dimensions. The red circle indicates the width of the quark brane. The blue circle indicates the width of the lepton brane. The black lines are black-holes traces. The size of the mini-bulk is  $10 \text{ TeV}^{-1} \times 10 \text{ TeV}^{-1}$ . black-holes with non-zero standard model gauge charges bounce back from the wall of the mini-bulk. black-holes with zero Standard Model gauge charges can leave the mini-bulk.

gluon-gluon or gluon-quark black-holes. The decline in the gluon-quark configurations accounts for the simultaneous rise in the fraction of quark-only configurations (*i.e.*  $3Q = 4, 1, -2$ ).

#### D. Initial Black-Hole Color Distribution

The colliding partons that form the black-hole carry gauge charges, in particular color and electromagnetic

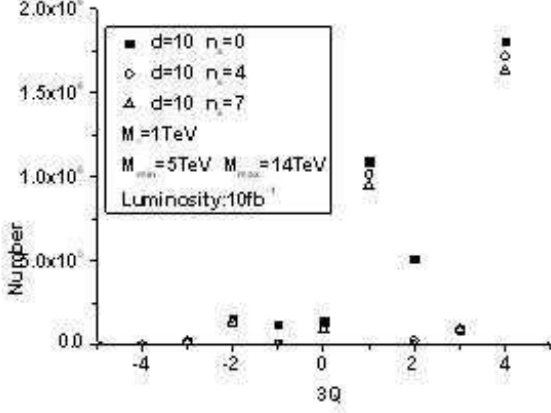


FIG. 25: Electromagnetic charge distribution of the initial black-holes.

charge. From the PDFs [32] we see that, at the relevant parton momentum, most of the partons are u and d type quarks – essentially the valence quarks. Contributions from “the sea” – other quarks, antiquarks, gluons and other partons – are subdominant. We therefore estimate the distribution of the colors of the initial black-holes to be

$$N_i(0) : N_i(1) : N_i(2) = 4 : 4 : 1. \quad (55)$$

Here  $N_i(p)$  is the number of black-holes whose  $i$ -th color-vector component ( $i=1$  is red,  $i=2$  blue,  $i=3$  green) has the value  $p$ . This agrees very well with the graph in Fig. 26.  $N_i(-1)$  and  $N_i(-2)$  refer to black-holes created from collisions involving gluons or anti-quarks. Their numbers are hard to estimate, but we expect that  $N_i(-2) \ll f_i(-1) \ll N_i(0 \leq p \leq 2)$ , again consistent with Fig. 26.

At energy scales accessible at the LHC, the color distribution of black-holes in different brane world models does not differ from each other significantly. However, were  $M_{min}$  significantly lower (at or below 1 TeV), then black-hole production by gluon-gluon scattering would be more important, significantly altering the color distribution, and making it more sensitive to fermion brane-splitting (which lowers the gluon-gluon contribution).

### E. Evolution of Black-Hole Color and Charge during the Hawking Radiation Phase

Figure 27 shows the color distribution of the black-holes which they accumulate during the evaporation phase. From equation 55, the expected average initial color of the black-holes is  $2/3$ . Since the colors of emitted particles are assigned randomly, we expect the cumulative color distribution (CCD) to be symmetric around  $2/3$  and peaked at the value. This is indeed what we find.

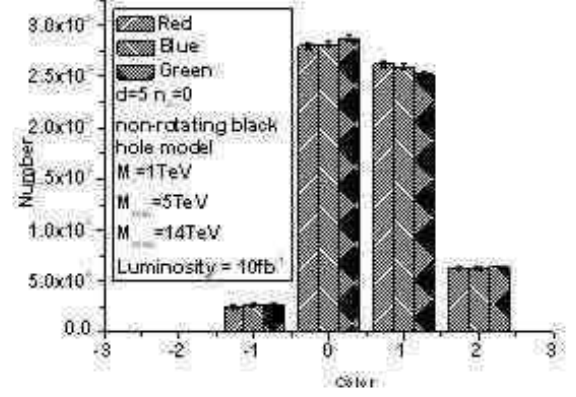


FIG. 26: Initial color distribution of the created black-holes. The vertical lines are error bar.

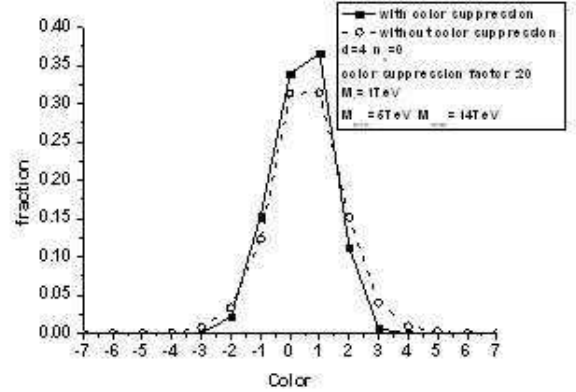


FIG. 27: Cumulative color distribution for non-rotating black-holes on a tensionless brane with  $d = 4$  and no fermion brane splitting. Histogram with the black squares (open circles) is with (without) color suppression.

The width of the CCD depends on the total number of particles emitted by the black-hole during its evaporation phase.

As discussed above, we allow for the possibility of suppressing particle emission which increases the charge, color or angular momentum of the black-hole excessively (cf. discussion around equations 37, and 52-54). Figure 27 shows also the cumulative black-hole color distribution where we suppressed the accumulation of large color charges during the evaporation phase. In order to amplify the effect of color suppression, we have set  $f_3 = 20$  instead of the expected  $f_3 \simeq 0.1$ . We see that the number of black-holes with a color charge larger than 1 is decreased.

## F. Number of emitted particles

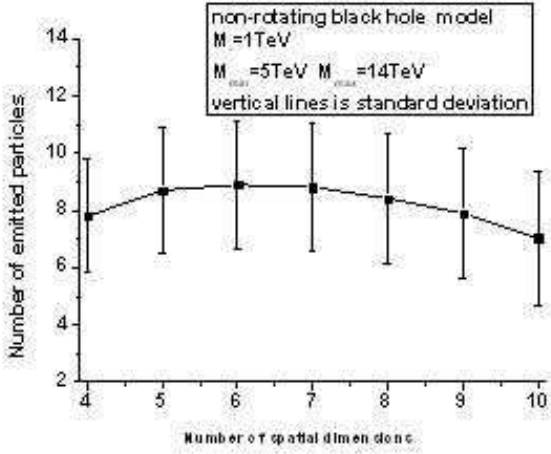


FIG. 28: Number of particles emitted by a non-rotating black-hole on a tensionless brane prior to the “final burst” as function of number of extra dimension. Here  $n_s = 0$ . The error bars denote one standard deviation range.

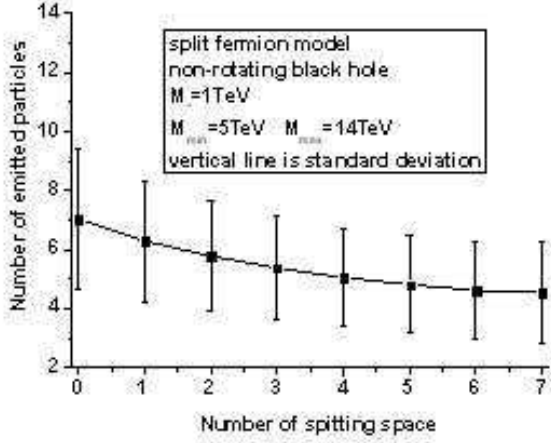


FIG. 29: Number of particles emitted by a non-rotating black-hole in the split-fermion model prior to the “final burst” as a function of the number of brane-splitting dimensions, with  $d = 10$ . Error bars denote one standard deviation range.

Figures 28 through 31 show the number of particles that are emitted by a microscopic black-hole during the decay process before its final burst for a variety of models.

In the single tensionless brane model (Fig. 28), the number of emitted particles first increases with the number of dimensions for a non-rotating black-hole, but then decreases. This behaviour is a result of the complicated interplay of a number of effects: the horizon size of a black-hole of a given mass as a function of  $d$ , and its

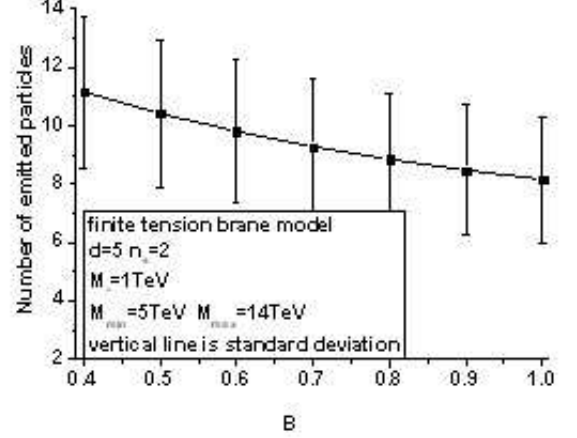


FIG. 30: Number of particles emitted by a non-rotating black-hole on a non-zero tension brane prior to the “final burst” as function of deficit angle parameter  $B$  with  $d = 5$  and  $n_s = 2$ . Error bars denote one standard deviation range.

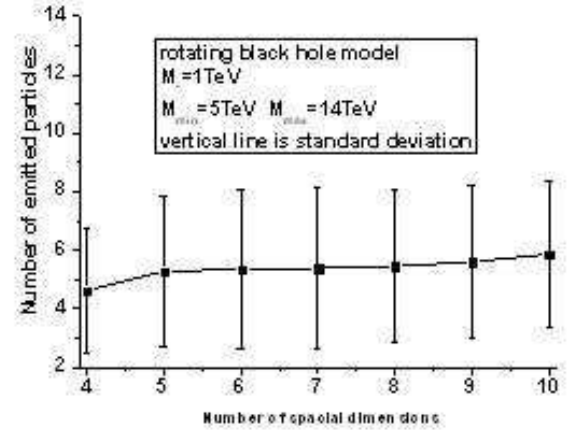


FIG. 31: Number of particles emitted by a rotating black-hole prior to the “final burst” as function of number of extra dimension with  $n_s = 0$ . Error bars denote one standard deviation range.

effect on the particle emission spectra; the dependence of the Hawking temperature on  $r_h^{(d)}$ ; the existence due to energy-momentum conservation of an upper limit of  $M^{bh}/2$  on the energy of an emitted particle. The location of the peak will shift as a function of the input parameter  $M_{min}$ , the minimum initial mass of a black-hole.

In the split fermion model (Fig. 29), the number of emitted particles decreases with the number of extra dimensions. This is because, even for a fixed Hawking temperature, the average energies of emitted gauge bosons and scalar fields increase as  $n_s$  increases.

In the model with a finite-tension brane (Fig. 30),

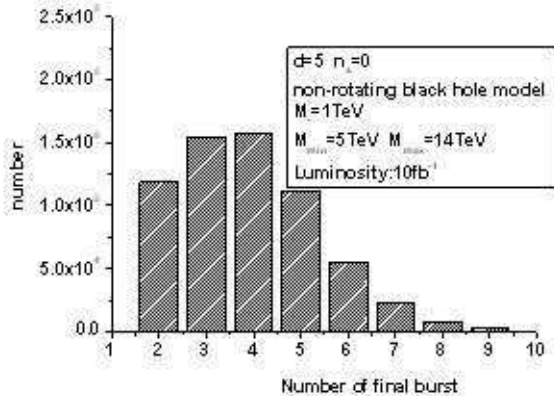


FIG. 32: Number of particles emitted at the final burst: the average number of final burst is about 3.4.

the number of particles decreases as the parameter  $B$  increases, *i.e.* with decreasing tension. As the tension increases,  $B$  gets smaller but the horizon radius of the black-hole increases. The Hawking temperature therefore decreases, and, as a consequence, the average energy of emitted particles falls. More particles will therefore be emitted in the evolution of the black-hole.

For rotating black-holes (Fig. 31) (on a tensionless, unsplit brane), the number of emitted particles first increases, then decreases, and finally reaches a plateau. This is due to similar reasons as for non-rotating black-holes. Compared to non-rotating black-holes of the same mass, rotation shifts the energy of emitted particles to higher values because it decreases the horizon radius and increases the emission of higher angular-momentum modes. This decreases the total number of emitted particles. It also means that the effect of the upper kinematic limit of  $M^{bh}/2$  on the emitted particle's energy is magnified.

Figure 32 shows the number of particles that are emitted at the final burst stage for a non-rotating black-hole on a tensionless brane with  $d = 5$  and  $n_s = 0$ . The average number of emitted particles is about 3. During the Hawking radiation phase a black-hole emits about 10 particles, so approximately 30% of the emitted particles will be from the final burst stage. In the case examined in Figure 32, we did not include suppression of large black-hole color or electric charge. Thus some black-holes acquire large color and electric charges by the end of the Hawking radiation phase. These black-holes then must decay into a large number of particles ( $> 5$ ) in the final burst.

## G. Energy Distributions of the Emitted Particles

Once formed, the black-holes decay by emission of Hawking radiation, a process which continues until the mass of the black-hole falls to the fundamental quantum-gravity scale. At this stage we chose the black-holes to burst into a set of Standard-Model particles as described in section V. The observable signatures of the decay will depend on the distributions of energy, momentum and particle types of the emitted particles.

Figures 33 through 36 show the relation between the mass of the evolving black-hole and the average energy of emitted particles for different extra dimension models. The error bars denote  $1/\sqrt{N}$  times the standard deviation of the mean energy. The minimum mass of the initial black-hole is taken to be  $M_{min} = 5 \text{ TeV}$ .

We see from figure 33 that, for a single (*i.e.* unsplit) brane, when  $M_{bh} \gg M_*$ , a black-hole in  $d = 10$  emits higher energy particles than a black-hole in lower dimensions. For black-hole masses closer to  $M_*$ , the highest energy particles are emitted when the dimensionality of space is low, *i.e.*  $d = 4$ . This reversal can be understood from figure 2. In the LHC energy range, the curves of Hawking temperature as a function of black-hole mass for different dimensions cross. At high mass, high  $d$  exhibits the highest Hawking temperature; at low mass, low  $d$  exhibits the highest Hawking temperature. It is easy from this figure to estimate the number of emitted particles, and to roughly reproduce the results shown in figure 28.

The main difference between the curves for different  $d$ , comes from the changing size of the black-hole horizon. For low  $d$ , the horizon radius increases more quickly with the mass than for higher  $d$ , as seen in figure 1. The Hawking temperature of the black-hole is inversely proportional to  $r_h$ . So long as the Hawking temperature remains well below the black-hole mass (here for  $M_{bh} \gtrsim 2\text{TeV}$ ), the energy of emitted particles decreases as the mass increases. However as equations (11-12) show, this change is slow for high  $d$ . By  $d = 10$ , the energy of emitted particles is almost constant from  $2\text{TeV}$  to  $5\text{TeV}$ .

The increase of the energy of emitted particles stops at about  $2\text{TeV}$  and then a decrease begins. The reason, as stated above (equation (32)), is that by energy-momentum conservation, a black-hole can only emit particles with less than half of its mass.

In the split-fermion model (Fig. 34), the average energy of the emitted particles increases as the number of dimensions in the mini-bulk increases. The energy shift comes from the gauge bosons and scalar fields, which access the higher-dimensional phase space of the mini-bulk (*cf.* appendix A: figure 50 through 61).

For the brane with non-zero tension (Fig. 35), the radius of the black-hole increases with tension hence the energy of emitted particles decreases with tension.

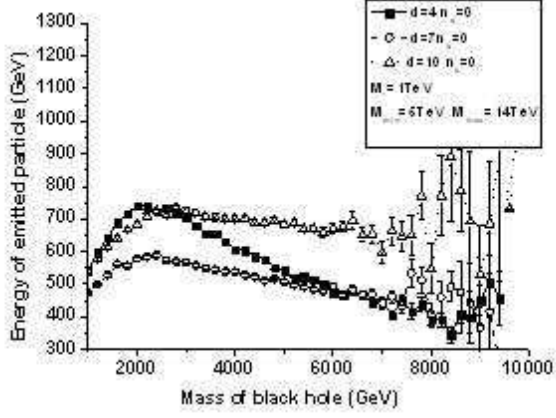


FIG. 33: Average energy of the particles emitted by (non-rotating) black-holes on unsplit branes versus the mass of the black-hole at the time of emission. Here  $d = 4$ ,  $d = 7$  and  $d = 10$ . Note that the final burst is not included, because it occurs when the mass of the black-hole is less than 1 TeV.

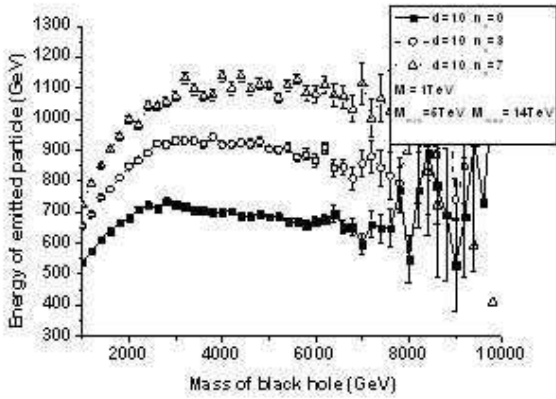


FIG. 34: Average energy of the particles emitted by (non-rotating) black-holes on split branes versus the mass of the black-hole at the time of emission. Here  $d = 10$  and  $n_s = 0$ ,  $n_s = 3$ ,  $n_s = 7$ .

For a rotating black-hole (Fig. 36), angular momentum decreases the size of the horizon. Thus since black-holes are typically formed with some initial angular momentum, they emit higher energy particles than non-rotating black-holes of the same mass. However, the black-hole tends to shed its angular momentum rapidly as it emits particles. This increases the horizon size, lowers the Hawking temperature, and lowers the average energy of the emitted particles. The rapid shedding of angular momentum thus leads to a drop in the average emitted particle energy around  $M_{\min}$ .

If one compares rotating with non-rotating black-holes, one finds that the energy of the emitted particles is always larger for the rotating black-holes. By the time

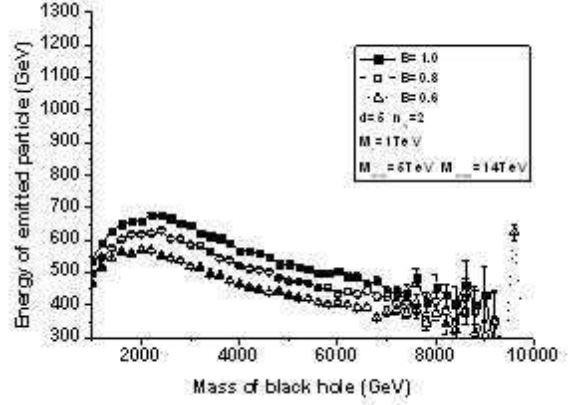


FIG. 35: Average energy of the particles emitted by (non-rotating) black-holes on a brane with tension, versus the mass of the black-hole at the time of emission. Here  $d = 5$ ,  $n_s = 2$  and  $B = 1$ ,  $B = 0.8$ ,  $B = 0.6$ .

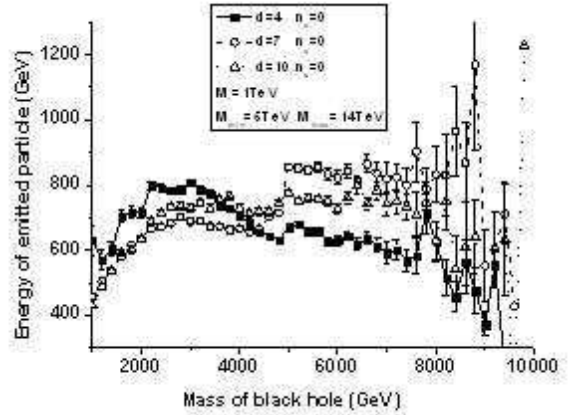


FIG. 36: Average energy of the particles emitted by (possibly rotating) black-holes versus the mass of the black-hole at the time of emission. Here  $d = 4$ ,  $d = 7$  and  $d = 10$ , with a tensionless unsplit brane.

the mass of the black-hole has dropped well below  $M_{\min}$  (here to approximately 1–2 TeV), almost all of the angular momentum has been lost and the difference between the rotating and non-rotating black-holes is small.

As a Standard-Model particle is emitted from a black-hole, this particle may carry some momentum in the extra dimensional directions. As an observer in 3-space observes this particle, he/she will find the apparent mass of the particle is

$$M_{ob} = \sqrt{M_p^2 + \sum_e P_e^2} \quad (56)$$

Here  $M_{ob}$  is the observed mass,  $M_p$  is the true mass of the particle, and  $P_e$  is the particles extra-dimensional

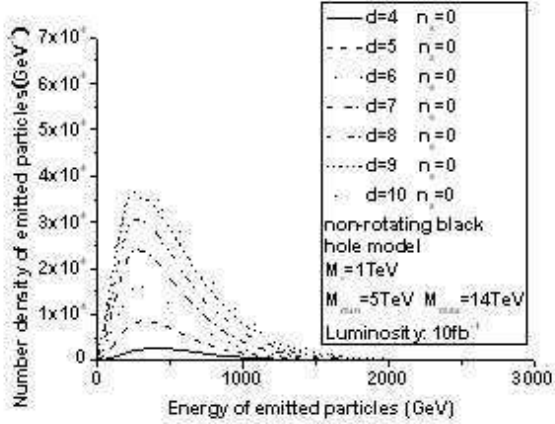


FIG. 37: Energy distribution of emitted particles in the Hawking radiation step for single-brane non-rotating black-hole.

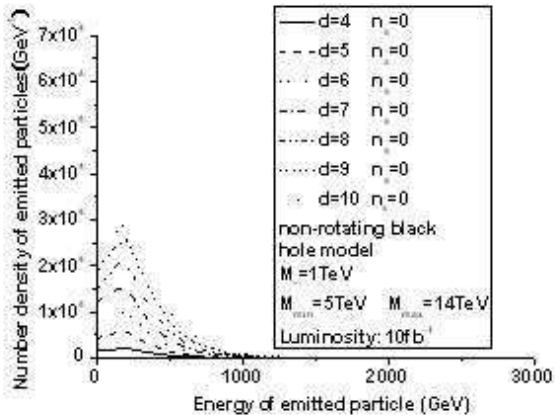


FIG. 38: Energy distribution of emitted particles at the final burst step for single-brane non-rotating black-hole.

momentum. Clearly  $M_{ob} \geq M_p$ . A Standard-Model particle, however, cannot leave the Standard Model brane. Its extra-dimensional momentum must therefore be absorbed by the brane or carried away by bulk particles (such as gravitons). We therefore calculate an emitted particle's "energy on the brane" according to:

$$E_b = \sqrt{M_p^2 + \sum_{i=1}^3 P_i^2} \quad (57)$$

where  $P_i$  is the regular 3-momentum. We will assume that the shedding of extra-dimensional momentum is rapid, and **henceforth** we will refer to  $E_b$  (rather than the initial emission energy) as the energy of the emitted particle.

Figure 37 shows the energy distribution of the particles from Hawking radiation in the single-brane model. The

cross section for black-hole production increases with  $d$  (figure 7). The area under the curves also increase with  $d$ . The peaks of the curves are around 200GeV to 400GeV. One can compare, for example, the energy distributions for  $d = 9$  and  $d = 10$ . A black-hole in high  $r$   $d$  tends to emit particles with higher energy, so the curve for  $d = 10$  has a longer higher energy tail than for  $d = 9$ .

Figure 38 shows the energy distribution of the particles from the final burst in the single-brane model. The energy these particles share is much smaller than the energy in the earlier Hawking radiation phase. The peak in the energy distribution of these particle is around 200GeV to 300GeV. The tails extend just to 1TeV, which is the mass at which the black hole is taken to be unstable and undergo its final burst.

Figures 39 through 42 show the energy distribution of emitted particles (including final burst particles) in the various models that BlackMax can simulate.

Figure 39 shows the energy distribution in the single-brane model. The cross section of black-hole increases with  $d$  (figure 7). The area under the curves also increases with  $d$ . The peaks of the curves are around 200 GeV to 400. Again comparing  $d = 9$  and  $d = 10$ , a black-hole in higher  $d$  tends to emit particles with higher energy, so the curve for  $d = 10$  has a longer high energy tail than for  $d = 9$ .

Figure 40 illustrates the split-fermion model. In this figure, we keep the total number of dimensions  $d$  fixed but change the dimensionality  $n_s$  of the mini-bulk. This affects the spectra of only the gauge boson and scalar fields, as only their propagation is affected by the the mini-bulk's dimensionality. (Gravitons propagate in the full bulk; other Standard-Model particles propagate only on the brane.) As explained above, these spectra will shift to higher energies as the number of splitting dimensions is increased. One can see that the curve in  $n_s = 7$  has the longest high energy tail.

Figure 41 illustrates the brane with tension model. The energies of the emitted particles shift to lower energy as  $B$  decreases.

The energy distribution of emitted particles for rotating black-holes (figure 42) has the same general characteristics as the distribution for non-rotating black-holes. Angular momentum causes a black-hole to tend to emit higher energy particles than a non-rotating black-hole. The curves have longer higher energy tails than the non-rotating black-holes.

Figure 43 shows the Energy distribution of emitted particles from two-body final-states scenario. The energy of the emitted particles is about the half of the incoming partons.

In figure 44 we show the energy distribution of different types of particles in the  $d = 5$  single-brane model. The area of each curve is dependent on the degree of freedom of each particle and its power spectrum. One can compare the ratio of the same type of particles. For example,

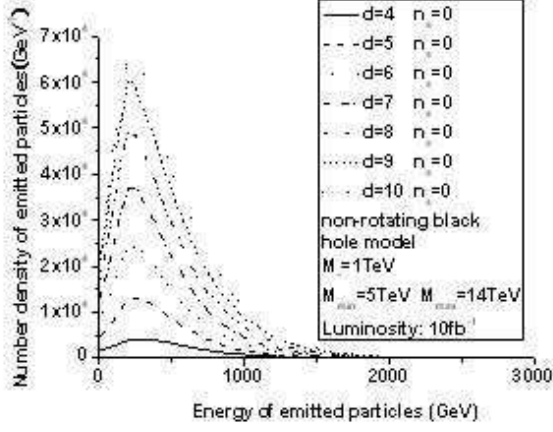


FIG. 39: Energy density distribution of emitted particles from non-rotating black-holes on a tensionless brane with no splitted fermion branes. Shown are the distributions for  $4 \leq d \leq 10$ . The spectra include the final burst particles.

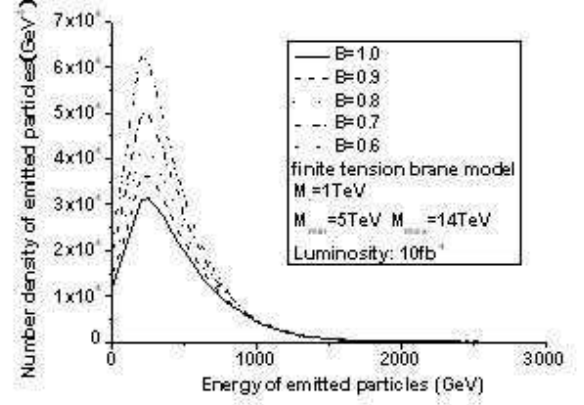


FIG. 41: Energy distribution of emitted particles for non-rotating black holes on a non-zero tension brane with  $B = 1$ ,  $B = 0.8$  and  $B = 0.6$ . The spectra include the final burst particles.

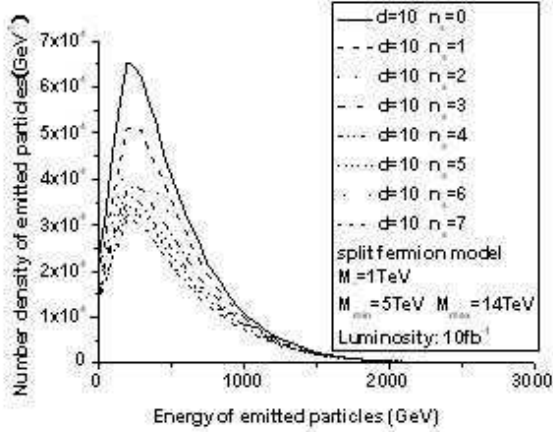


FIG. 40: Energy density distribution of emitted particles from non-rotating black-holes on a tensionless brane with fermion brane splitting. Shown are the distributions for  $d = 10$  and  $0 \leq n_s \leq 7$ . The spectra include the final burst particles.

the area of gluons should be 8 times as large as the area of photons. It is roughly the same as what the figure shows.

#### H. Pseudorapidity Distributions of the Emitted Particles

Figures 45 to 48 show the pseudorapidity distributions of the emitted particles for different extra dimension scenarios.

Most of black-holes are made of two  $u$  quarks and have charge  $3/4$ . For the shown figures we did not include

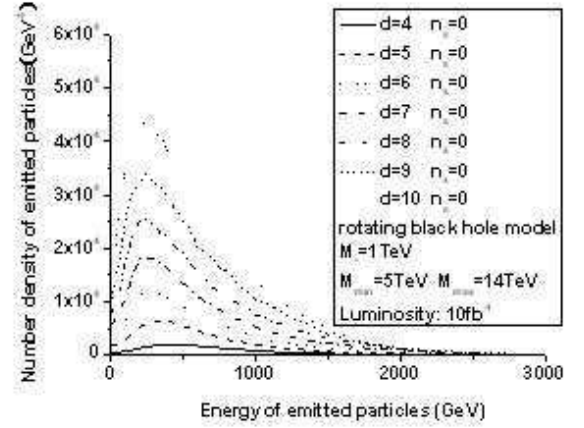


FIG. 42: Energy distribution of emitted particles for rotating black-holes for  $4 \leq d \leq 10$ .

charge suppression, because of that the black-holes tend to emit the same number of particles and antiparticles during Hawking radiation phase. This can be seen from the curves without final burst in figure 45 through figure 48. The majority of the black-holes are positive charged and will tend to emit positive particles in the final burst. That is why there are more positrons than electrons for the distributions which include the final burst particles.

Figure 49 shows the pseudorapidity distribution in the two-body final-state scenario. The distribution is much wider than the equivalent distribution from Hawking radiation. In this model we do not consider the angular momentum of the black hole. We therefore take the decay process in the two-body final state scenario to be isotropic in the ordinary spatial directions, just as in other models without angular momentum. In the center



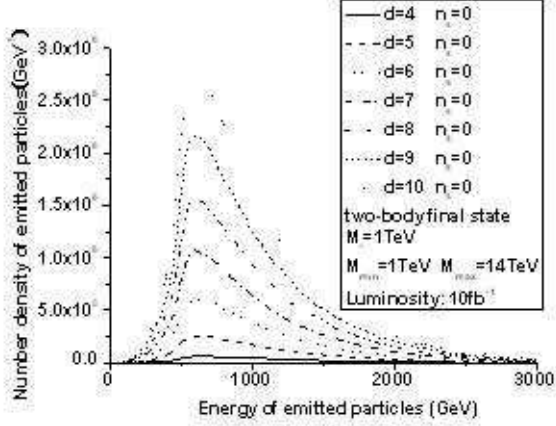


FIG. 43: Energy distribution of emitted particles for two-body final states.

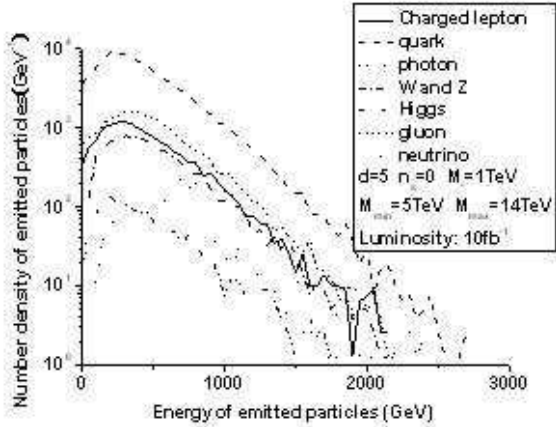


FIG. 44: Energy distribution of each particle type in the  $d = 5$  single brane model.

of mass frame, particles are therefore emitted in directions uncorrelated with the beam direction. Nevertheless, because the threshold energy of the two-body final-state model is much lower than that of other models, the intermediate state tends to have a higher velocity down the beam-pipe. The decay products are therefore emitted with larger pseudorapidity. In truth, one may expect that the intermediate state of the two-body final-state scenario has non-negligible angular momentum. However, since the intermediate state is not a real black hole, it is unclear exactly what role the angular momentum of the intermediate state plays.

In the final state scenario, the momenta of the two emitted particles are correlated with the initial parton momenta, and hence the pseudorapidity distribution of the emitted particles reflects that of the initial partons. The ratio of the number of events for pseudorapidity be-

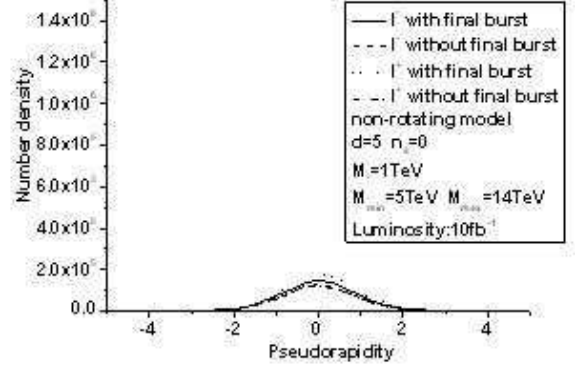


FIG. 45: Pseudorapidity distribution of charge leptons and anti leptons for non-rotating black-holes on a tensionless brane with and without the final burst particles;  $d = 5$ .

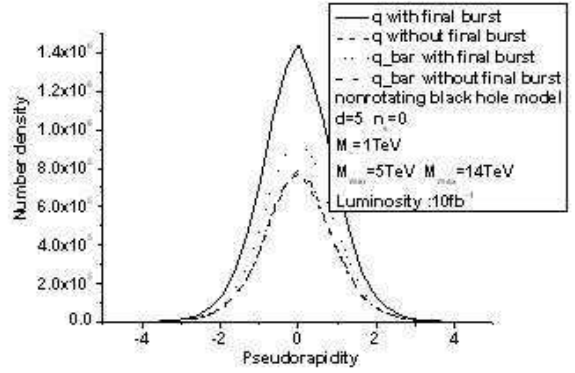


FIG. 46: Pseudorapidity distribution of quarks and anti quarks for non-rotating black-holes on a tensionless brane with and without the final burst particles;  $d = 5$ .

tween 0 and 0.5 divided by that for pseudorapidity between 0.5 and 1 is about 1.1. This is much higher than the asymptotic QCD value of 0.6, as predicted by [16, 26]. If the ratio is found not to equal 0.6, then this would suggest new physics beyond the Standard Model.

## I. Emitted Particle Types

Table III shows, for a variety of representative extra-dimension scenarios the fraction of emitted particles which are of each possible type – quarks, gluons, (charged) leptons, (weak) gauge bosons, neutrinos, gravitons, Higgs bosons and photons. One notable feature is that the intensity of gravitons relative to other particles increases with the number of extra dimensions. Note that the absence of gravitons in the case of a rotating black-hole is *not* physical, but rather reflects our ignorance of the correct gray-body factor.

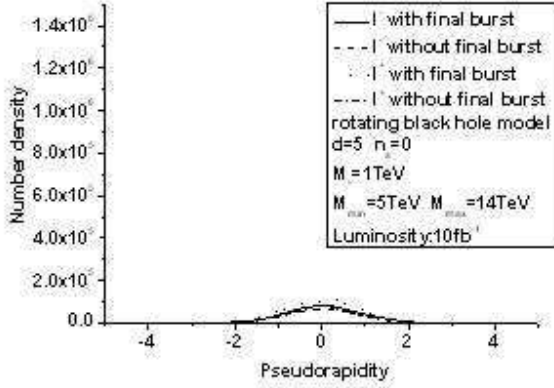


FIG. 47: Pseudorapidity distribution of charged leptons and anti-leptons for rotating black-holes, on a tensionless brane, with and without the final burst particles. Here  $d = 5$ .

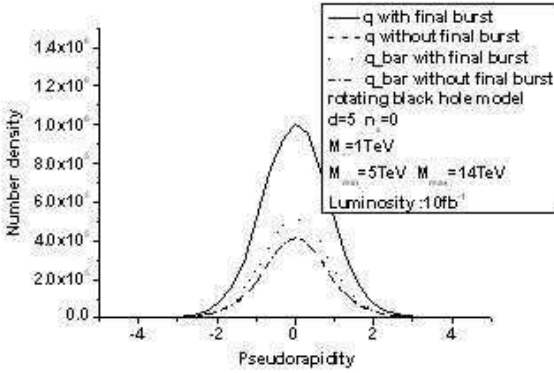


FIG. 48: Pseudorapidity distribution of quarks and anti-quarks for rotating black-holes, on a tensionless brane, with and without the final burst particles. Here  $d = 5$ .

VIII. CONCLUSION

Hitherto, black-hole generators for the large-extra-dimension searches at the LHC have made many simplifying assumptions regarding the model of both our three-dimensional space and the extra-dimensional space, and simplifying assumptions regarding the properties of the black-holes that are produced. In this paper we have discussed a new generator for black-holes at the LHC, BlackMax, which removes many of these assumptions. With regard to the extra-dimensional model it allows for brane tension, and brane splitting. With regard to the black-hole, it allows for black-hole rotation, charge (both electro-magnetic and color) and bulk recoil. It also introduces the possibility of a two-body final state that is not a black-hole.

Although BlackMax represents a major step forward, there remain important deficiencies that will need to be

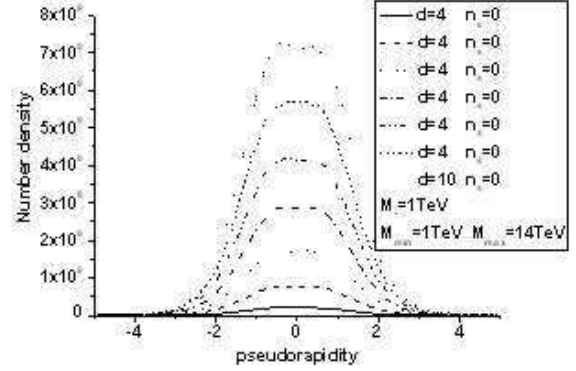


FIG. 49: Pseudorapidity distribution for the two-body final-state scenario. The distribution in 2-body final states is much flatter near  $\eta = 0$  than emission due to Hawking radiation.

addressed in the future. BlackMax continues to insist on a flat geometry for the bulk space, whereas there is considerable interest in a warped geometry [3] or in a compact hyperbolic geometry [4]. While BlackMax allows for black-hole rotation, the absence of either an analytic or a numerical gray-body factor for the graviton in more than three space dimensions for rotating black-holes is a *serious* shortcoming that can be expected to materially change the signature of black-hole decay for rotating black-holes. Other issues include how to properly account for the likely suppression of decays that cause a black-hole to acquire very “large” color, charge or angular momentum. (As opposed to the somewhat contrived phenomenological approach currently taken.) These are but a few of the fundamental issues that remain to be clarified.

Despite these (and no doubt other) shortcomings, we expect that BlackMax will allow for a much improved understanding of the signatures of black-holes at the LHC. Work in progress focuses on using BlackMax to explore the consequences for the ATLAS experiment of more realistic black-hole and extra-dimension models.

We thank Nicholas Brett for discussions in the early stages of this paper. We thank Daisuke Ida, Kin-ya Oda, and Seong Chan Park for providing some of the spectra of rotating black-holes. DCD, DS and GDS thank Oxford’s Atlas group for its hospitality at various stages of this project. DCD, DS and GDS have been supported in part by a grant from the US DOE; GDS was supported in part by the John Simon Guggenheim Memorial Foundation and by Oxford’s Beecroft Institute for Particle Astrophysics and Cosmology.

[1] <http://www-pnp.physics.ox.ac.uk/~issever/BlackMax/blackmax.html>

- [2] Nima Arkani-Hamed, Savas Dimopoulos, G.R. Dvali, Phys. Rev. D59:086004, 1999. hep-ph/9807344. Ignatios Antoniadis, Nima Arkani-Hamed, Savas Dimopoulos, G.R. Dvali, Phys. Lett. B436:257-263, 1998. hep-ph/9804398. Nima Arkani-Hamed, Savas Dimopoulos, G.R. Dvali, Phys. Lett. B429:263-272, 1998. hep-ph/9803315.
- [3] Lisa Randall, Raman Sundrum, Phys.Rev.Lett.83:4690-4693,1999. hep-th/9906064.
- [4] N. Kaloper, J. March-Russell, G. D. Starkman and M. Trodden, Phys. Rev. Lett. **85**, 928 (2000) [arXiv:hep-ph/0002001]; G. D. Starkman, D. Stojkovic and M. Trodden, Phys. Rev. Lett. **87**, 231303 (2001) [arXiv:hep-th/0106143]. G. D. Starkman, D. Stojkovic and M. Trodden, Phys. Rev. D **63**, 103511 (2001) [arXiv:hep-th/0012226].
- [5] I. Antoniadis, Phys. Lett. B **246**, 377 (1990); K. R. Dienes, E. Dudas and T. Gherghetta, Phys. Lett. B **436**, 55 (1998) [arXiv:hep-ph/9803466].
- [6] T. Banks, W. Fischler, hep-th/9906038 ; S. Dimopoulos, G. Landsberg, Phys. Rev. Lett. **87** 161602 (2001) ; S. B. Giddings and S. Thomas, Phys. Rev. **D65** 056010 (2002)
- [7] K. S. Thorne, Nonspherical gravitational collapse: A short review. In J R Klauder, Magic Without Magic, San Francisco 1972, 231-258; D. Ida and K.-i. Nakao, Phys. Rev. D66 (2002)064026, [gr-qc/0204082]; H. Yoshino and Y. Nambu, Phys. Rev. D66 (2002)065004, [gr-qc/0204060].
- [8] T. Vachaspati, D. Stojkovic and L. M. Krauss, Phys. Rev. D **76**, 024005 (2007) [arXiv:gr-qc/0609024]. T. Vachaspati and D. Stojkovic, arXiv:gr-qc/0701096.
- [9] TRUENOIR: Savas Dimopoulos, Greg L. Landsberg, Phys. Rev. Lett. 87:161602,2001. hep-ph/0106295  
CHARYBDIS: C.M. Harris, P. Richardson, B.R. Webber, JHEP 0308:033, 2003. hep-ph/0307305.  
Catfish: M. Cavaglia, R. Godang, L. Cremaldi, D. Summers, hep-ph/0609001.
- [10] D. C. Dai, G. D. Starkman and D. Stojkovic, Phys. Rev. D **73**, 104037 (2006) [arXiv:hep-ph/0605085]; D. Stojkovic and G. D. Starkman, D. C. Dai, Phys. Rev. Lett. **96**, 041303 (2006) [arXiv:hep-ph/0505112]
- [11] D. Stojkovic, F. C. Adams and G. D. Starkman, Int. J. Mod. Phys. D **14**, 2293 (2005) [arXiv:gr-qc/0604072]; C. Bambi, A. D. Dolgov and K. Freese, Nucl. Phys. B **763**, 91 (2007) [arXiv:hep-ph/0606321]; arXiv:hep-ph/0612018.
- [12] N. Arkani-Hamed, M. Schmaltz, Phys. Rev. **D61** 033005 (2000)
- [13] Ya. B. Zel'dovich, Pis'ma v Zh. Eksp. Teor. Fiz. 12, 443; Ya. B. Zel'dovich, Sov. Phys. JETP Lett. 14, 180; Ya. B. Zel'dovich, Sov. Phys. JETP 35, 1085; C. W. Misner, Phys. Rev. Lett. 28, 994 (1972); V. P. Frolov, D. Stojkovic, Phys. Rev. **D67** 084004 (2003); Phys. Rev. **D68** 064011 (2003)
- [14] Nemanja Kaloper, Derrick Kiley, JHEP 0603:077,2006. hep-th/0601110
- [15] De-Chang Dai, Nemanja Kaloper, Glenn D. Starkman, Dejan Stojkovic. Phys. Rev. D75:024043,2007. hep-th/0611184
- [16] Patrick Meade, Lisa Randall, arXiv:0708.3017 [hep-ph]
- [17] Vitor Cardoso, Marco Cavaglia, Leonardo Gualtieri. JHEP 0602:021,2006. hep-th/0512116
- [18] Christopher Michael Harris. Ph.D. thesis. hep-ph/0502005
- [19] Chris M. Harris, Panagiota Kanti. JHEP 0310:014,2003. hep-ph/0309054
- [20] G. Duffy, C. Harris, P. Kanti, E. Winstanley. JHEP 0509:049,2005. hep-th/0507274
- [21] C.M. Harris, P. Kanti. Phys.Lett.B633:106-110,2006. hep-th/0503010
- [22] M. Casals, P. Kanti, E. Winstanley. JHEP 0602:051,2006. hep-th/0511163
- [23] M. Casals, S.R. Dolan, P. Kanti, E. Winstanley. JHEP 0703:019,2007. hep-th/0608193
- [24] Daisuke Ida, Kin-ya Oda, and Seong Chan Park, Phys. Rev. **D73**, 124022 (2006), hep-th/0602188
- [25] S. Creek, O. Efthimiou, P. Kanti and K. Tamvakis, Phys. Rev. D **75**, 084043 (2007) [arXiv:hep-th/0701288]; arXiv:0707.1768 [hep-th] T. Harmark, J. Natario and R. Schiappa, arXiv:0708.0017 [hep-th].
- [26] B. Abbott *et al.* [D0 Collaboration], Phys. Rev. Lett. **82**, 2457 (1999) [arXiv:hep-ex/9807014].
- [27] D. Stojkovic, Phys. Rev. Lett. **94**, 011603 (2005) [arXiv:hep-ph/0409124].
- [28] Luis A. Anchordoqui, Jonathan L. Feng, Haim Goldberg, Alfred D. Shapere, Phys.Lett.B594:363-367,2004. hep-ph/0311365
- [29] V. Frolov, D. Stojkovic, Phys. Rev. Lett. **89** 151302 (2002); Phys. Rev. **D66** 084002 (2002); D. Stojkovic, Phys.Rev.Lett. **94** 011603 (2005)
- [30] D. Stojkovic, JHEP 0409:061 (2004)
- [31] D. Ida, K. Oda, S. C. Park, Phys.Rev.**D67** 064025 (2003) Erratum-ibid.**D69** 049901 (2004)
- [32] J. Pumplin *et al.* JHEP 0207, 012 (2002)[hep-ph/0201195]; D. Stump *et al.*, JHEP 0310, 046 (2003)[hep-ph/0303013].
- [33] A. Flachi, O. Pujolas, M. Sasaki, T. Tanaka, hep-th/0601174; A. Flachi, T. Tanaka, Phys. Rev. Lett. **95** 161302 (2005)
- [34] T. G. Rizzo, hep-ph/0601029; hep-ph/0510420; JHEP **0501** 028 (2005)
- [35] D.K. Park, hep-th/0512021; hep-th/0511159
- [36] M. Casals, P. Kanti, E. Winstanley, hep-th/0511163
- [37] R. da Rocha, C. H. Coimbra-Araujo, JCAP **0512** 009 (2005)
- [38] A.S. Cornell, W. Naylor, M. Sasaki; hep-th/0510009
- [39] J. Grain, A. Barrau, P. Kanti, Phys.Rev.**D72** 104016 (2005)
- [40] H. Yoshino, T. Shiromizu, M. Shibata, Phys.Rev. **D72** 084020 (2005)
- [41] G. Duffy, C. Harris, P. Kanti, E. Winstanley, JHEP **0509** 049 (2005)
- [42] E. Jung, D.K. Park, Nucl.Phys. **B731** 171 (2005)
- [43] L. Lonnblad, M. Sjudahl, T. Akesson, JHEP **0509** 019 (2005)
- [44] J.I. Illana, M. Masip, D. Meloni, Phys.Rev.**D72** 024003 (2005)
- [45] E. Jung, S. Kim, D.K. Park, Phys.Lett. **B619** 347 (2005); Phys.Lett. **B614** 78 (2005)
- [46] H. Yoshino, V. S. Rychkov, Phys.Rev. **D71** 104028 (2005)
- [47] A.S. Majumdar, N. Mukherjee, Int.J.Mod.Phys. **D14** 1095 (2005); astro-ph/0403405; Mod. Phys. Lett. **A 20**, 2487 (2005).
- [48] A. Perez-Lorenzana, hep-ph/0503177
- [49] D. Ida, K. Oda, S. C. Park, Phys.Rev. **D71** 124039

- (2005);hep-th/0602188
- [50] V. P. Frolov, D. V. Fursaev, D. Stojkovic, *Class. Quant. Grav.* **21** 3483 (2004); *JHEP* **0406** 057 (2004);
- [51] A.N. Aliev, A.E. Gumrukcuoglu, *Phys.Rev.* **D71** 104027 (2005); A.N. Aliev, gr-qc/0505003; A.N. Aliev, V. P. Frolov, *Phys.Rev.***D69** 084022 (2004)
- [52] P. Kanti, J. Grain, A. Barrau, *Phys.Rev.* **D71** 104002 (2005); P. Kanti, K. Tamvakis, *Phys.Rev.* **D65** 084010 (2002); P. Kanti, J. March-Russell, *Phys.Rev.***D67** 104019 (2003); P. Kanti, *Int.J.Mod.Phys.***A19** 4899 (2004)
- [53] H. Yoshino, Y. Nambu, *Phys.Rev.* **D70** 084036 (2004)
- [54] E. F. Eiroa, gr-qc/0511004; *Phys.Rev.* **D71** 083010 (2005)
- [55] P. S. Apostolopoulos, N. Brouzakis, E. N. Saridakis, N. Tetradis *Phys.Rev.* **D72** 044013 (2005)
- [56] S. Creek, O. Eftimiou, P. Kanti, K. Tamvakis, hep-th/0601126
- [57] D. Stojkovic, *Phys.Rev.***D67** 045012 (2003)
- [58] E. Berti, V. Cardoso, M. Casals, *Phys.Rev.* **D73** 024013 (2006)
- [59] M. Vasudevan, K. A. Stevens, *Phys.Rev.* **D72** 124008 (2005)
- [60] B. M.N. Carter, I. P. Neupane, *Phys.Rev.* **D72** 043534 (2005)
- [61] L. Lonnblad, M. Sjodahl, T. Akesson, *JHEP* **0509** 019 (2005)
- [62] V. Frolov, M. Snajdr and D. Stojkovic, *Phys. Rev.* **D68** 044002 (2003);
- [63] M. Nozawa, K. Maeda, *Phys.Rev.* **D71** 084028 (2005)
- [64] C. M. Harris, hep-ph/0502005
- [65] Y. Morisawa, D. Ida, *Phys.Rev.***D71** 044022 (2005)
- [66] V. Cardoso, O.J.C. Dias, J. P.S. Lemos, *Phys.Rev.***D67** 064026 (2003); V. Cardoso, O. J.C. Dias, J. L. Hovdebo, R. C. Myers, hep-th/0512277
- [67] A. Cafarella, C. Coriano, T.N. Tomaras, hep-ph/0412037
- [68] A. Chamblin, F. Cooper, G. C. Nayak, *Phys.Rev.* **D70** 075018 (2004); *Phys.Rev.* **D69** 065010 (2004)
- [69] D. Ida, Y. Uchida, Y. Morisawa, *Phys.Rev.***D67** 084019 (2003)
- [70] E.J. Ahn, M. Cavaglia, hep-ph/0511159
- [71] M. Cavaglia, S. Das, *Class.Quant.Grav.* **21** 4511 (2004); M. Cavaglia, S. Das, R. Maartens, *Class.Quant.Grav.* **20** L205 (2003)
- [72] V. Cardoso, M. Cavaglia, L. Gualtieri, hep-th/0512116
- [73] L. A. Anchordoqui, J. L. Feng, H. Goldberg, A. D. Shapere, *Phys.Lett.***B594** 363 (2004); L. Anchordoqui, H. Goldberg, *Phys.Rev.***D67** 064010 (2003); L. Anchordoqui, T. Han, D. Hooper, S. Sarkar, hep-ph/0508312
- [74] A. Casanova, E. Spallucci, *Class.Quant.Grav.* **23** R45 (2006)
- [75] J. E. Aman, N. Pidokrajt, *Phys.Rev.***D73** 024017 (2006)
- [76] U. Harbach, M. Bleicher, hep-ph/0601121
- [77] B. Koch, M. Bleicher, S. Hossenfelder, *JHEP* **0510** 053 (2005); S. Hossenfelder, *Phys.Lett.* **B598** 92 (2004)
- [78] M. Fairbairn, hep-ph/0509191
- [79] G.L. Alberghi, R. Casadio, D. Galli, D. Gregori, A. Tronconi, V. Vagnoni, hep-ph/0601243
- [80] P. Davis, hep-th/0602118; P. Krtous, J. Podolsky, *Class.Quant.Grav.* **23** 1603 (2006)
- [81] K.A. Bronnikov, S.A. Kononogov, V.N. Melnikov, gr-qc/0601114
- [82] B. Koch, M. Bleicher and H. Stoecker, arXiv:hep-ph/0702187.
- [83] S. Chen, B. Wang and R. K. Su, *Phys. Lett. B* **647**, 282 (2007) [arXiv:hep-th/0701209].
- [84] H. T. Cho, A. S. Cornell, J. Doukas and W. Naylor, *Phys. Rev. D* **75**, 104005 (2007) [arXiv:hep-th/0701193].
- [85] L. h. Liu, B. Wang and G. h. Yang, arXiv:hep-th/0701166.
- [86] B. Koch, arXiv:0707.4644 [hep-ph].
- [87] H. Stoecker, *J. Phys. G* **32**, S429 (2006).
- [88] B. Betz, M. Bleicher, U. Harbach, T. Humanic, B. Koch and H. Stoecker, arXiv:hep-ph/0606193.
- [89] A. N. Aliev, *Phys. Rev. D* **75**, 084041 (2007) [arXiv:hep-th/0702129].
- [90] T. G. Rizzo, *Phys. Lett. B* **647**, 43 (2007) [arXiv:hep-ph/0611224].
- [91] D. M. Gingrich, *Int. J. Mod. Phys. A* **21**, 6653 (2006) [arXiv:hep-ph/0609055]; arXiv:0706.0623 [hep-ph].
- [92] E. Abdalla, C. B. M. Chirenti and A. Saa, arXiv:gr-qc/0703071.
- [93] G. L. Landsberg, *J. Phys. G* **32**, R337 (2006) [arXiv:hep-ph/0607297].
- [94] H. Yoshino and R. B. Mann, *Phys. Rev. D* **74**, 044003 (2006) [arXiv:gr-qc/0605131].
- [95] Y. i. Takamizu, H. Kudoh and K. i. Maeda, *Phys. Rev. D* **75**, 061304 (2007) [arXiv:gr-qc/0702138].
- [96] R. da Rocha and C. H. Coimbra-Araujo, *Phys. Rev. D* **74**, 055006 (2006) [arXiv:hep-ph/0607027].
- [97] S. Creek, R. Gregory, P. Kanti and B. Mistry, *Class. Quant. Grav.* **23**, 6633 (2006) [arXiv:hep-th/0606006].
- [98] A. Perez-Lorenzana, *J. Phys. Conf. Ser.* **18**, 224 (2005) [arXiv:hep-ph/0503177].
- [99] A. Lopez-Ortega, *Gen. Rel. Grav.* **39**, 1011 (2007) [arXiv:0704.2468 [gr-qc]].
- [100] H. K. Kunduri, J. Lucietti and H. S. Reall, *Phys. Rev. D* **74**, 084021 (2006) [arXiv:hep-th/0606076].
- [101] H. T. Cho, A. S. Cornell, J. Doukas and W. Naylor, *Phys. Rev. D* **75**, 104005 (2007) [arXiv:hep-th/0701193].
- [102] S. B. Giddings, arXiv:0709.1107 [hep-ph].
- [103] S. Creek, O. Eftimiou, P. Kanti and K. Tamvakis, arXiv:0709.0241 [hep-th].
- [104] S. Chen, B. Wang and R. K. Su, arXiv:0710.3240 [hep-th].
- [105] A. Barrau, J. Grain and C. Weydert, arXiv:0710.1998 [hep-th].
- [106] U. A. al-Binni and G. Siopsis, arXiv:0708.3363 [hep-th].
- [107] D. Kiley, arXiv:0708.1016 [hep-th].

#### Appendix A: Particle Emission Spectra

Nowadays gray-body factors can be found in many papers. We collect the relevant papers in table I. We follow these papers to calculate energy power spectra in our database except for the split-fermions model (although we independently confirm the results as well). We perform an original calculation of the spectra of gauge bosons and scalar fields in the split-fermions model as

a function of the number of dimensions  $n_s$  in which the fermion branes are split. These are shown in figures 50 to 61.

Anyone who has a better spectrum can upgrade our database. For example, we only calculate the spectra up to the  $l = 9$  mode.

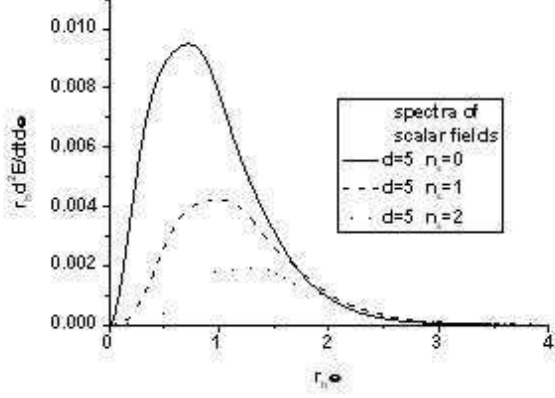


FIG. 50: Spectra of scalar fields in d=5 space.

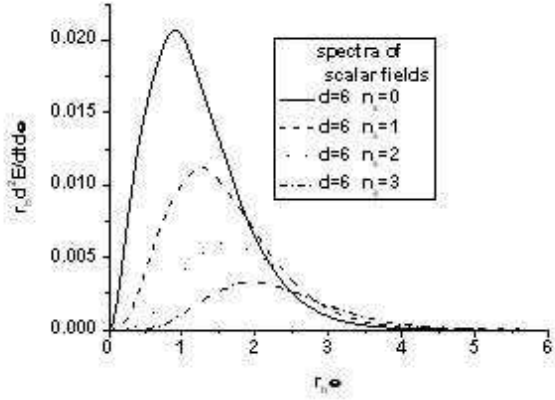


FIG. 51: Spectra of scalar fields in d=6 space.

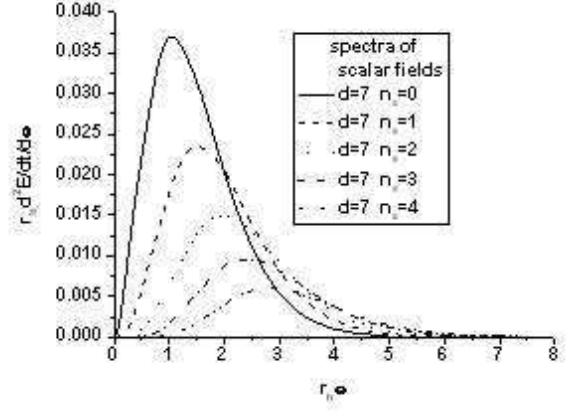


FIG. 52: Spectra of scalar fields in d=7 space.

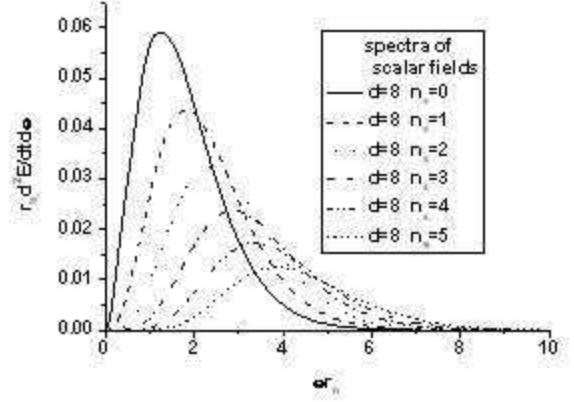


FIG. 53: Spectra of scalar fields in d=8 space.

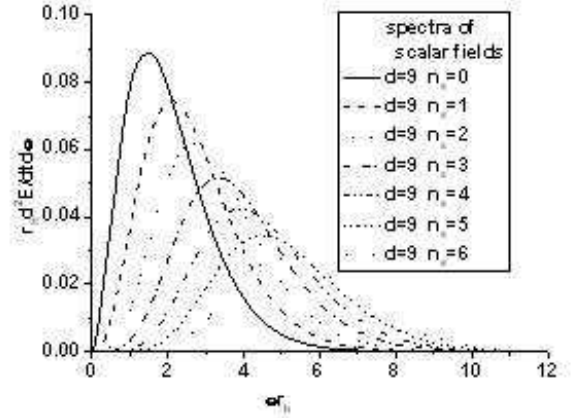


FIG. 54: Spectra of scalar fields in d=9 space.

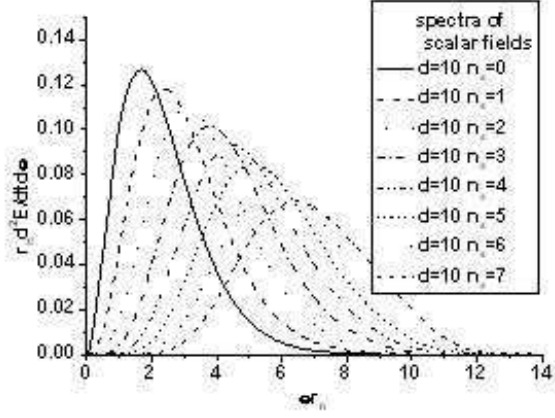


FIG. 55: Spectra of scalar fields in d=10 space.

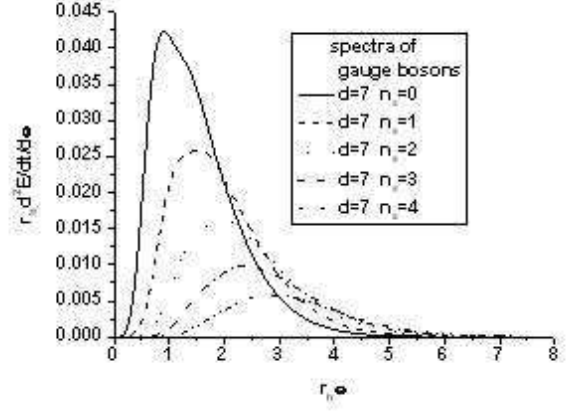


FIG. 58: Spectra of gauge bosons in d=7 space.

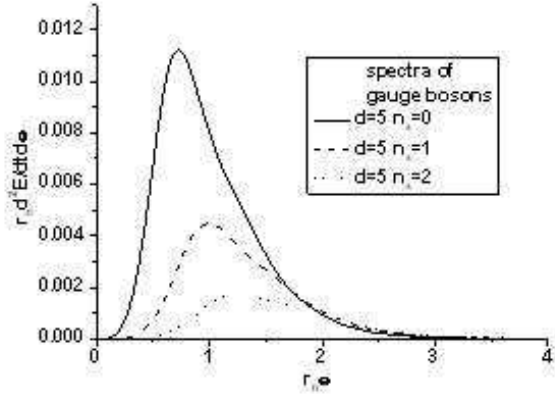


FIG. 56: Spectra of gauge bosons in d=5 space.

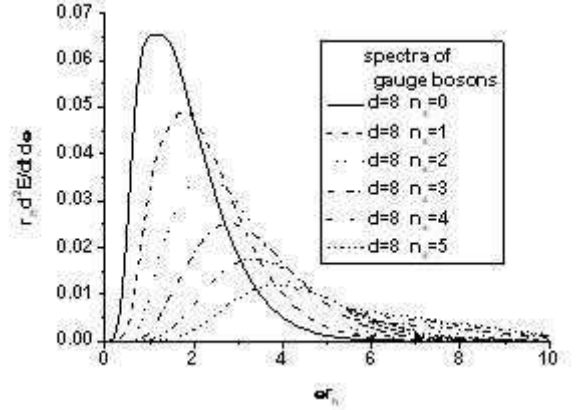


FIG. 59: Spectra of gauge bosons in d=8 space.

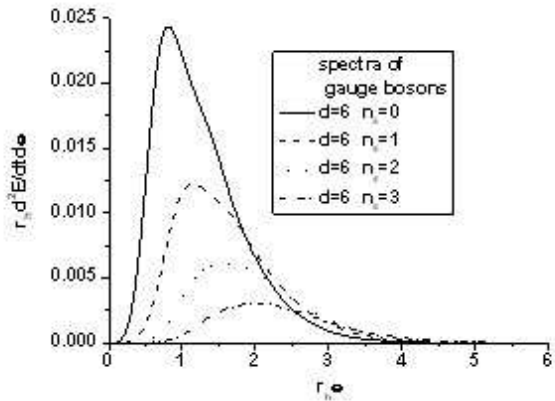


FIG. 57: Spectra of gauge bosons in d=6 space.

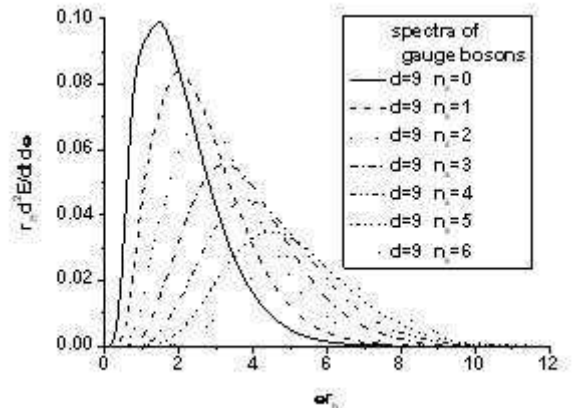


FIG. 60: Spectra of gauge bosons in d=9 space.

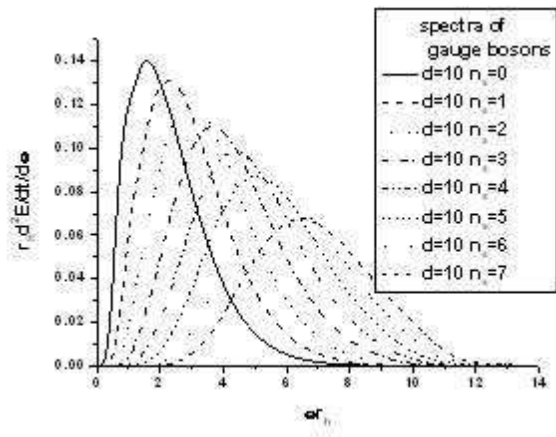


FIG. 61: Spectra of gauge bosons in  $d=10$  space.

TABLE I: Literature sources for particle emission spectra

| Type of particle         | Type of black hole | Brane model                 | References        |
|--------------------------|--------------------|-----------------------------|-------------------|
| Standard-Model particles | non-rotating       | unsplit; tensionless        | [18][19]          |
| gravitons                | non-rotating       | split/unsplit; tensionless  | [17]              |
| Standard-Model particles | non-rotating       | split/unsplit; with tension | [15]              |
| gravitons                | non-rotating       | split/unsplit; with tension | [15]              |
| scalars and gauge bosons | non-rotating       | split; tensionless          | figures 50-61     |
| fermions                 | rotating           | unsplit; tensionless        | [23][24]          |
| gauge bosons             | rotating           | unsplit; tensionless        | [22][24]          |
| scalar fields            | rotating           | unsplit; tensionless        | [18] [20][21][24] |

TABLE II: Degrees of freedom of Standard-Model particles which are emitted from a black hole. For gravitons, the table shows 1, because the appropriate growth in the number of degrees of freedom is included explicitly in the graviton emission spectrum.  $n_s$  is the number of extra dimensions in which vector and scalar fields can propagate.

| particle type     | $d_0$ | $d_{1/2}$ | $d_1$        | $d_2$ |
|-------------------|-------|-----------|--------------|-------|
| Quarks            | 0     | 6         | 0            | 0     |
| Charged leptons   | 0     | 2         | 0            | 0     |
| Neutrinos         | 0     | 2         | 0            | 0     |
| Photons or gluons | 0     | 0         | $2 + n_s$    | 0     |
| $Z^0$             | 1     | 0         | $2 + n_s$    | 0     |
| $W^+$ and $W^-$   | 2     | 0         | $2(2 + n_s)$ | 0     |
| Higgs boson       | 1     | 0         | 0            | 0     |
| Graviton          | 0     | 0         | 0            | 1     |



TABLE III: The fraction of emitted particles of different types (including final burst particles) in a variety of extra dimension scenarios. \*Note that the absence of gravitons in the case of a rotating black hole is due exclusively to our current ignorance of the correct gray-body factor.

| Scenario  | quarks | gluons | leptons | gauge bosons | neutrinos | gravitons | Higgs bosons | photons  |
|---|--------|--------|---------|--------------|-----------|-----------|--------------|----------|
| $d = 4$ $n_s = 0$ non-rotating black hole       | 68.21  | 10.79  | 9.45    | 5.72         | 3.87      | 2.00e-01  | 8.99e-01     | 8.61e-01 |
| $d = 5$ $n_s = 0$ non-rotating black hole       | 65.37  | 13.29  | 9.04    | 6.12         | 3.76      | 4.60e-01  | 8.26e-01     | 1.13     |
| $d = 6$ $n_s = 0$ non-rotating black hole       | 63.63  | 14.51  | 8.93    | 6.58         | 3.51      | 7.59e-01  | 7.76e-01     | 1.30     |
| $d = 7$ $n_s = 0$ non-rotating black hole       | 61.25  | 15.94  | 8.75    | 7.17         | 3.45      | 1.20      | 7.89e-01     | 1.44     |
| $d = 8$ $n_s = 0$ non-rotating black hole       | 60.99  | 15.94  | 8.56    | 6.99         | 3.35      | 1.93      | 7.63e-01     | 1.47     |
| $d = 9$ $n_s = 0$ non-rotating black hole       | 59.40  | 16.26  | 8.26    | 7.08         | 3.26      | 3.48      | 7.45e-01     | 1.51     |
| $d = 10$ $n_s = 0$ non-rotating black hole      | 57.56  | 16.15  | 7.68    | 6.82         | 3.17      | 6.46      | 6.97e-01     | 1.46     |
| $d = 10$ $n_s = 1$ split fermions model         | 61.58  | 19.76  | 1.64    | 7.30         | 3.83e-01  | 6.95      | 5.88e-01     | 1.80     |
| $d = 10$ $n_s = 2$ split fermions model         | 61.28  | 20.40  | 1.66    | 7.09         | 3.49e-01  | 6.91      | 4.56e-01     | 1.86     |
| $d = 10$ $n_s = 3$ split fermions model         | 62.10  | 20.33  | 1.65    | 6.76         | 4.46e-01  | 6.43      | 4.15e-01     | 1.87     |
| $d = 10$ $n_s = 4$ split fermions model         | 62.70  | 19.76  | 1.72    | 6.60         | 4.66e-01  | 6.62      | 3.28e-01     | 1.80     |
| $d = 10$ $n_s = 5$ split fermions model         | 63.67  | 19.34  | 1.73    | 6.14         | 5.17e-01  | 6.50      | 2.65e-01     | 1.83     |
| $d = 10$ $n_s = 6$ split fermions model         | 64.96  | 18.24  | 1.82    | 5.85         | 5.56e-01  | 6.69      | 2.35e-01     | 1.65     |
| $d = 10$ $n_s = 7$ split fermions model         | 66.38  | 17.23  | 1.83    | 5.44         | 5.50e-01  | 6.68      | 2.51e-01     | 1.64     |
| $d = 2$ $n_s = 2$ $B = 1.0$ tension brane model | 84.13  | 9.39   | 1.66    | 2.80         | 2.02e-01  | 9.23e-01  | 2.51e-01     | 6.30e-01 |
| $d = 2$ $n_s = 2$ $B = 0.9$ tension brane model | 85.33  | 8.88   | 1.65    | 2.49         | 1.63e-01  | 7.55e-01  | 1.90e-01     | 5.47e-01 |
| $d = 2$ $n_s = 2$ $B = 0.8$ tension brane model | 86.42  | 8.32   | 1.54    | 2.32         | 1.79e-01  | 5.70e-01  | 1.99e-01     | 4.49e-01 |
| $d = 2$ $n_s = 2$ $B = 0.7$ tension brane model | 87.06  | 7.93   | 1.63    | 2.08         | 1.75e-01  | 5.19e-01  | 1.98e-01     | 4.00e-01 |
| $d = 2$ $n_s = 2$ $B = 0.6$ tension brane model | 87.92  | 7.39   | 1.60    | 1.94         | 1.59e-01  | 4.46e-01  | 1.88e-01     | 3.59e-01 |
| $d = 2$ $n_s = 2$ $B = 0.5$ tension brane model | 88.51  | 7.11   | 1.46    | 1.84         | 1.33e-01  | 3.96e-01  | 1.86e-01     | 3.67e-01 |
| $d = 2$ $n_s = 2$ $B = 0.4$ tension brane model | 89.16  | 6.58   | 1.58    | 1.72         | 1.49e-01  | 3.54e-01  | 1.66e-01     | 2.90e-01 |
| $d = 4$ $n_s = 0$ rotating black hole           | 64.82  | 15.41  | 7.94    | 6.25         | 3.50      | 0.00*     | 6.06e-01     | 1.48     |
| $d = 5$ $n_s = 0$ rotating black hole           | 61.38  | 18.11  | 7.89    | 7.06         | 3.30      | 0.00*     | 5.56e-01     | 1.70     |
| $d = 6$ $n_s = 0$ rotating black hole           | 59.21  | 20.38  | 7.27    | 7.59         | 3.08      | 0.00*     | 5.85e-01     | 1.89     |
| $d = 7$ $n_s = 0$ rotating black hole           | 57.52  | 21.82  | 7.08    | 8.08         | 2.87      | 0.00*     | 5.77e-01     | 2.05     |
| $d = 8$ $n_s = 0$ rotating black hole           | 54.41  | 24.02  | 6.75    | 9.09         | 2.77      | 0.00*     | 6.07e-01     | 2.36     |
| $d = 9$ $n_s = 0$ rotating black hole           | 51.88  | 24.05  | 7.98    | 9.27         | 3.55      | 0.00*     | 7.15e-01     | 2.55     |
| $d = 10$ $n_s = 0$ rotating black hole          | 52.43  | 25.67  | 6.45    | 9.62         | 2.52      | 0.00*     | 6.79e-01     | 2.63     |
| $d = 4$ $n_s = 0$ two-body final states         | 58.88  | 16.89  | 1.38    | 6.08         | 11.14     | 0.00e+00  | 1.91         | 3.71     |
| $d = 5$ $n_s = 0$ two-body final states         | 57.71  | 17.46  | 1.37    | 6.22         | 11.53     | 0.00e+00  | 1.91         | 3.80     |
| $d = 6$ $n_s = 0$ two-body final states         | 57.16  | 17.72  | 1.39    | 6.27         | 11.59     | 0.00e+00  | 1.93         | 3.94     |
| $d = 7$ $n_s = 0$ two-body final states         | 57.02  | 17.91  | 1.37    | 6.22         | 11.59     | 0.00e+00  | 1.98         | 3.91     |
| $d = 8$ $n_s = 0$ two-body final states         | 56.58  | 18.08  | 1.35    | 6.31         | 11.79     | 0.00e+00  | 1.92         | 3.97     |
| $d = 9$ $n_s = 0$ two-body final states         | 56.51  | 18.02  | 1.41    | 6.40         | 11.75     | 0.00e+00  | 1.96         | 3.95     |
| $d = 10$ $n_s = 0$ two-body final states        | 56.66  | 18.06  | 1.43    | 6.28         | 11.74     | 0.00e+00  | 1.92         | 3.90     |